

*SiPM Gain calibration
for the scintillating Cosmic Ray Tracker*

*Master thesis
Faculty of Sciences, University of Bern*

*Submitted by
Pablo Vergés
2016*

Supervisor
Prof. Dr. Igor Kreslo

The silicon photomultiplier (SiPM)'s gain and its dependency on the bias voltage is studied and used to improve the distribution of gains within a Cosmic Ray Tracker (CRT) module.

The distribution of gains is displayed before and after calibration.

Further studies on the CRT modules with varying power supply and bias voltages are presented.

Contents

<i>Introduction</i>	5
<i>What is the standard model of particle physics?</i>	6
<i>The neutrino, from proposal to discovery</i>	6
<i>What are neutrino's properties?</i>	8
<i>Neutrino detection</i>	9
<i>Counting atoms</i>	9
<i>Observing chain interactions</i>	9
<i>Cherenkov detectors</i>	10
<i>Bubble & cloud chambers</i>	10
<i>Photoemulsion films</i>	10
<i>Time projection chambers</i>	11
<i>Neutrino interactions</i>	12
<i>Currents of the weak interaction</i>	12
<i>Energy-momentum transfer and event classification</i>	12
<i>Elastic & quasi-elastic scattering</i>	13
<i>Neutrino sources</i>	15
<i>Natural sources</i>	15
<i>Other sources</i>	15
<i>Neutrino oscillations and anomalies in the observations</i>	16
<i>Neutrino oscillation models</i>	16
<i>Two flavor oscillation probabilities in vacuum</i>	17
<i>Matter effects</i>	18
<i>Anomalies in neutrino oscillation observations</i>	19
<i>Liquid Scintillator Neutrino Detector</i>	19
<i>MiniBooNE</i>	19
<i>Short Baseline Neutrino Program</i>	20
<i>The Booster Neutrino Beam line</i>	20
<i>MicroBooNe</i>	21
<i>Short-Baseline Near Detector</i>	21
<i>Electron neutrino signals from cosmic background</i>	22
<i>Cosmic rays</i>	22
<i>Interactions contributing to the neutrino signal</i>	23
<i>The Cosmic Ray Tagger</i>	24
<i>The Cosmic Ray Tagger in a nutshell</i>	24
<i>Background mitigation</i>	25

<i>The Cosmic Ray Tagger panel</i>	26
<i>The panel in a nutshell</i>	26
<i>Aluminium shielding</i>	27
<i>Scintillating bars</i>	28
<i>Wavelength shifting fibers</i>	29
<i>Silicon photomultiplier</i>	30
<i>The Cosmic Ray Tracker Front-End Board</i>	31
<i>The Front-End Board in a nutshell</i>	31
<i>Bias voltage generator</i>	31
<i>Triggering logic</i>	32
<i>Analog signal readout and digitization</i>	32
<i>Event data structure & storage</i>	33
<i>The Front-End Board software</i>	33
<i>Calibration of a Cosmic Ray Tagger module</i>	34
<i>The signal spectrum</i>	34
<i>Determine the gain of a silicon photomultiplier</i>	35
<i>Dependency of the gain on the bias voltage</i>	37
<i>The spectra of an uncalibrated panel vs. a calibrated panel</i>	38
<i>Further studies on the Cosmic Ray Tracker</i>	40
<i>Sets of observations</i>	40
<i>Effects of changing power supply voltages on the pedestal</i>	40
<i>Influences of the power supply voltage on the spectrum</i>	41
<i>Event rate vs. power supply voltages</i>	41
<i>Effects of changing bias voltages on the pedestal</i>	43
<i>Conclusions</i>	46
<i>Bibliography</i>	49

Introduction

The main goal of this project is to calibrate the gain for the scintillating CRT modules with the aim to improve the uncertainty of its efficiency.

Since this project is highly motivated by the study of neutrinos, a brief introduction into neutrinos, their detection, interactions, oscillations, the effects which arise when neutrinos travel through matter and the currently running Short-Baseline Neutrino (SBN) program is made.

To motivate the usage of the CRT, the neutrino signal from the cosmic background is discussed and how the CRT helps identifying part of this signal.

The CRT is presented along with its components, dedicating one section to the determination of the gain, its calibration process and results.

Further observations of the data are made as side studies in the last section, to study the behaviour of the CRT under different conditions and show the versatility of the developed tools.

The rest of this section aims to introduce the Standard Model (SM) and neutrinos by referencing breakthroughs in the history of neutrino physics.

... you can skip this chapter and watch Boris Kayser's Public Neutrino lecture instead: Neutrinos Get Under Your Skin

What is the standard model of particle physics?

The SM of particle physics is a theory which describes electromagnetic, weak and strong nuclear interactions and classifies all the known subatomic particles. The SM has demonstrated continued successes in predicting and explaining a wide variety of experimental results¹. Yet it does leave some phenomena without explanation and it does not incorporate general relativity. For this reasons it is sometimes regarded as the “theory of almost everything”.

Gravitation – the fourth known fundamental force of physics – is not included in the SM.

¹ Herrero, M. The Standard model: Techniques and Concepts of High-Energy Physics. *NATO Sci. Ser. C*, 534: 1–59, 1999

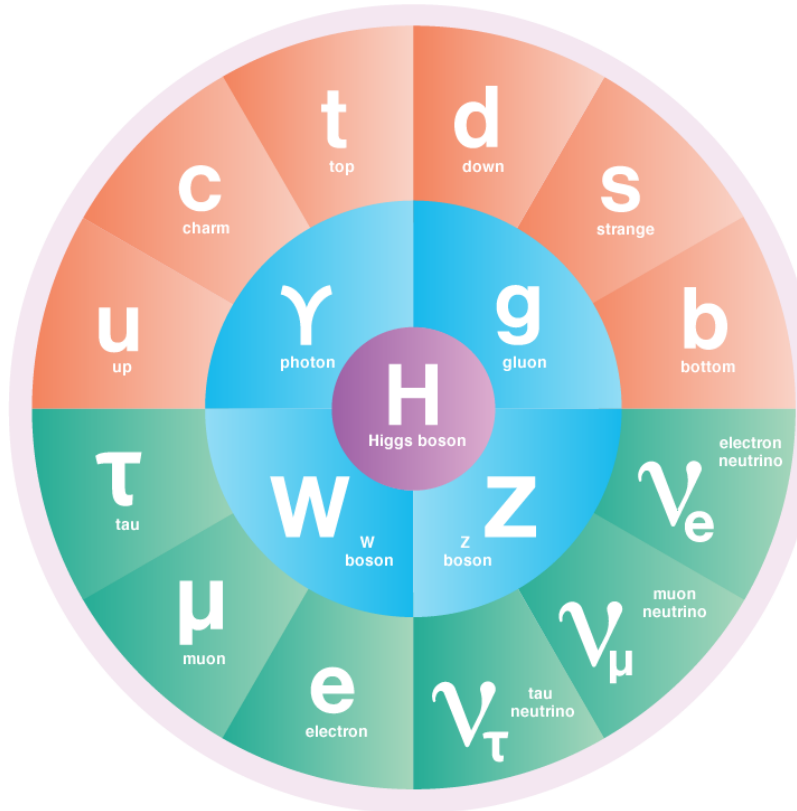


Figure 1: The particles of the SM are divided into subsets: quarks (orange), leptons (green), gauge bosons (blue) and the Higgs boson (violet). The up-like quarks (u, c, t) carry a charge of $\frac{2}{3}e$, while the down-like quarks (d, s, b) charge is $-\frac{1}{3}e$. The three leptons on the left (e, μ, τ) have the charge $-e$, while the leptons on the right (ν_e, ν_μ, ν_τ) are neutral. The gauge bosons are the mediators of electromagnetism (γ), weak interaction (W^\pm, Z) and strong interaction (g). The Higgs boson (H) is responsible for the SM fermions' mass. – ©symmetrymagazine.org

Mathematically speaking, the SM is a gauge quantum field theory built upon internal symmetries of the unitary product group $SU(3) \times SU(2) \times U(1)$.

The neutrino, from proposal to discovery

Pauli proposed the existence of a neutral particle with almost no mass in 1930² to describe the continuous energy spectrum of β -decays without breaking the principle of energy conservation. His spin $\frac{1}{2}$, neutral, light particle was practically undetectable, such that he considered his idea not to be in stage of publication. Enrico Fermi developed a theory of β -decays based on Pauli's idea and introduced the name neutrino. Supported by Fermi's theory, Pauli presented his idea in 1933.

The experimental proof of the existence of the neutrino was provided in 1956 by Frederick Reines' and Clyde L. Cowan, Jr.'s. The

Unitary and special unitary groups of degree 1, 2 and 3

² Brown, L. M. The idea of the neutrino. *Physics Today*, 31:23–28, sep 1978

It took 23 years to proof the existence of neutrinos!

setup consisted of water tanks, liquid scintillator, photomultipliers, an efficient neutron absorber and some logic signal treatment. Measuring a very characteristic signature of the inverse β -decay, led to a drastical reduction of the background³. This made it possible to get significant results, placing the setup close to a nuclear reactor.

³ Frederick Reines. Nobel Lecture: The Neutrino: From Poltergeist to Particle, dec 1995. URL http://www.nobelprize.org/nobel_prizes/physics/laureates/1995/reines-lecture.html



The Argonne National Laboratory run the Zero Gradient Synchrotron from 1963 to 1979 and used a 12-foot hydrogen bubble chamber to record events from the accelerated particles and their byproducts. Using this technology, it was possible to register the world's first neutrino observation on November 13th 1970, displayed in figure 2. This event is the irrefutable proof of neutrino's existence.

Figure 2: World's first neutrino observation (Nov. 13th 1970) – ©Argonne National Laboratory

What are neutrino's properties?

Despite the development of neutrino detectors over the last decades, some neutrino properties remain yet unknown. Studying the properties of a particle is a good way to check our model's consistency or lead us to new, unknown physics. This is a good reason to keep developing and running neutrino experiments.

Classification in the SM As proposed by Pauli, neutrinos are neutral particles of small mass with spin 1/2 and therefore fermions. Neutrinos conserve leptonic number, making them part of the group of leptons. Neutrinos come in 3 different flavors, and each flavor is associated to one of the heavier leptons: electron neutrino ν_e , muon neutrino ν_μ and tauon neutrino ν_τ . The number of different light neutrino types was determined by studying Z-Boson production and decay⁴.

Helicity A handy way to group particles is by projecting a particle's spin along its direction of motion getting as a result its helicity. Particles with a positive helicity are called right-handed, their counterpart is called left-handed. So far there's no experimental evidence for right-handed neutrinos or left-handed antineutrinos^{5,6}. The first hints for neutrino's helicity were given T.D. Lee and C.N. Yang. They predicted in 1956 parity violation in weak interactions, by expressing the weak interaction as a chiral gauge interaction. This was later shown by Chien-Shiung Wu in collaboration with the Low Temperature Group of the US National Bureau of Standards⁷.

Mass Bruno Pontecorvo and Vladimir Gribov had an idea, which predicted that neutrinos undergo changes in flavor, called neutrino oscillations⁸. Raymond Davis Jr. and John Bahcall's solar neutrino problem strongly indicated the existence of neutrino oscillations and Takaaki Kajita and Arthur B. McDonald confirmed this with their experiment. Neutrino oscillations require neutrinos to have a non-zero mass and allow to study neutrino's relative mass. On the other hand the absolute mass of the three flavors of neutrinos remains unknown, such that different hierarchies are possible. At the point of writing, two possible hierarchies are considered: the normal hierarchy and the inverted hierarchy.

Neutrino velocities Due to their small mass, neutrinos generated in particle physics processes are expected to have velocities close to the one of light in vacuum. The velocity of neutrinos was measured in several experiments, confirming the theory's expectations^{9,10}.

⁴ D. Karlen. The number of light neutrino types from collider experiments. 2004

⁵ I. Sahin. A hypothesis on neutrino helicity. 2015

⁶ R. Romero. On the nature of the neutrino. *Mod. Phys. Lett.*, A31(19), 2016

⁷ C. S. Wu, E. Ambler, R. W. Hayward, D. D. Hoppes, and R. P. Hudson. Experimental test of parity conservation in beta decay. *Phys. Rev.*, 105:1413–1415, Feb 1957. doi: 10.1103/PhysRev.105.1413. URL <http://link.aps.org/doi/10.1103/PhysRev.105.1413> further developed by Ziro Maki, Masami Nakagawa and Shoichi Sakata

⁸ John Bahcall. Solving the mystery of the missing neutrinos, April 2004. URL http://www.nobelprize.org/nobel_prizes/themes/physics/bahcall/ The SM gives mass to fermions by the interaction with the Higgs field, which involves interactions with particles of both chiralities. Since no right-handed neutrinos and left-handed antineutrinos were observed so far, it is not clear where the neutrino masses arise from.

So called hot matter

⁹ M. Antonello et al. Precision measurement of the neutrino velocity with the icarus detector in the cngs beam. *JHEP*, 11:049, 2012

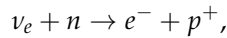
¹⁰ T. Adam et al. Measurement of the neutrino velocity with the opera detector in the cngs beam. *JHEP*, 10:093, 2012

Neutrino detection

You cannot see a neutrino directly, but if it interacts with a particle in our detector, we might observe and identify the byproducts of the interaction. A few techniques to determine neutrino fluxes and study neutrino's interactions with other particles have been developed. This section lists some of these methods.

Counting atoms

When neutrinos interact with the neutrons in the atom, a lepton and a proton may be produced



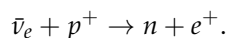
changing the nuclear structure and chemical properties of the atom it interacted with. If a tank is filled with pure homoatomic liquid and one is able to detect and count the resulting new atoms of the neutrino interactions, one can draw conclusions on the neutrinos and the neutrino flux. If the production rate of neutrinos can be controlled, as it is the case with nuclear reactors, the results are even more evident. And even though counting the number of atoms seems a difficult process, a number of experiments prove that it is feasible.

Chemists know how to do this!

Like the experiment run by John Bahcall and Raymond Davis Jr.

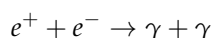
Observing chain interactions

One could observe the subsequent reactions of the byproducts of the neutrino interaction to conclude a neutrino interaction. A clear signal raising from the background is needed for this cause. For instance, the interaction of an electron antineutrino and a proton results in a neutron and a positron



This astute technique was used by Clyde Cowan and Frederick Reines to detect electron antineutrinos.

The positron won't travel very far in matter until it annihilates with an electron, emitting two photons



with an energy of approximately half an MeV in opposite directions. If the neutron is absorbed by the nucleus of some atom, the latter may react. When cadmium absorbs a neutron, it'll go into a metastable state, which decays into its ground state by emitting a gamma ray



In a center of mass system, the photons' energy will be equivalent to the electron and positron's mass.

The time window from the neutrino interaction to the electron positron annihilation and the gamma emission of the nucleus is a determinant characteristic of the process.

Cherenkov detectors

No particle faster than the speed of light in vacuum was found so far. But light's speed depends on the refractive index of the medium it is travelling through. Therefore charged particles can travel through a suitable medium faster than light does, producing *Cherenkov radiation*, a measurable cone of light. This light can be read out to reconstruct the geometry of the cone and identify the particle which generated it. Such cones are displayed in the illustrations of figure 3. Kamiokande, Liquid Scintillator Neutrino Detector (LSND), MiniBooNE and many other detectors used this technique.

Physicists call these hypothetical particles *tachions*.

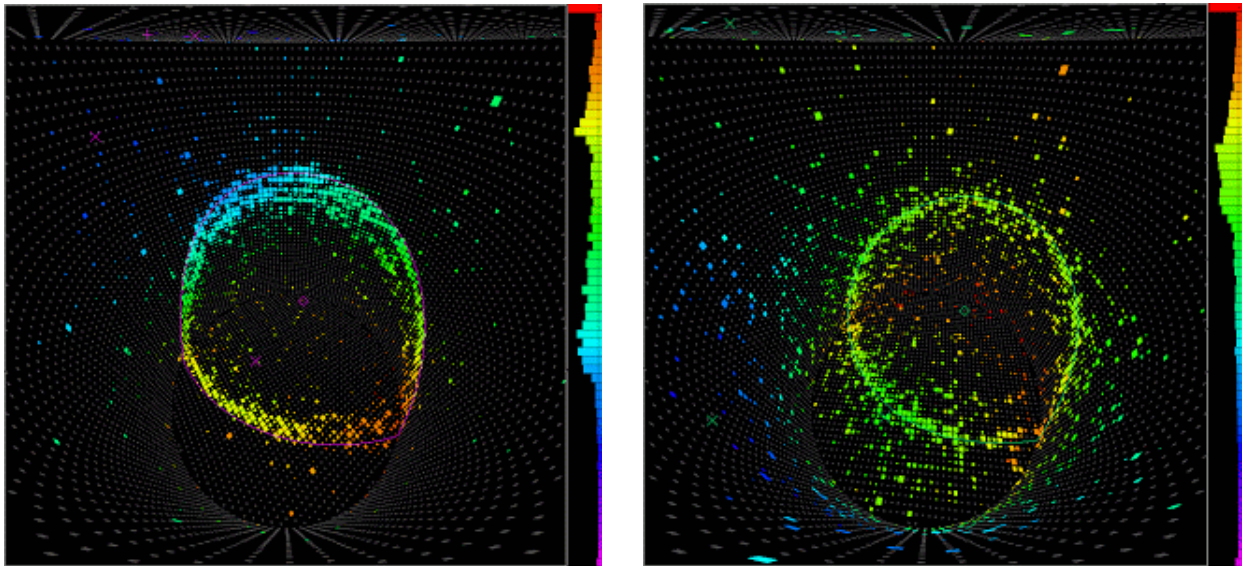


Figure 3: Images of events in Super Kamiokande. The illustration on the left shows a muon event, the one on the right an electron event. The muon's cone has a clean shape while the electron's cone is less evident. Electrons scatter more than muons, due to their lower mass, leading to a spread cone. The time scale on the right displays the time window and energy deposit during the observation. – ©Tomasz Barszczak - Super-Kamiokande Collaboration

Bubble & cloud chambers

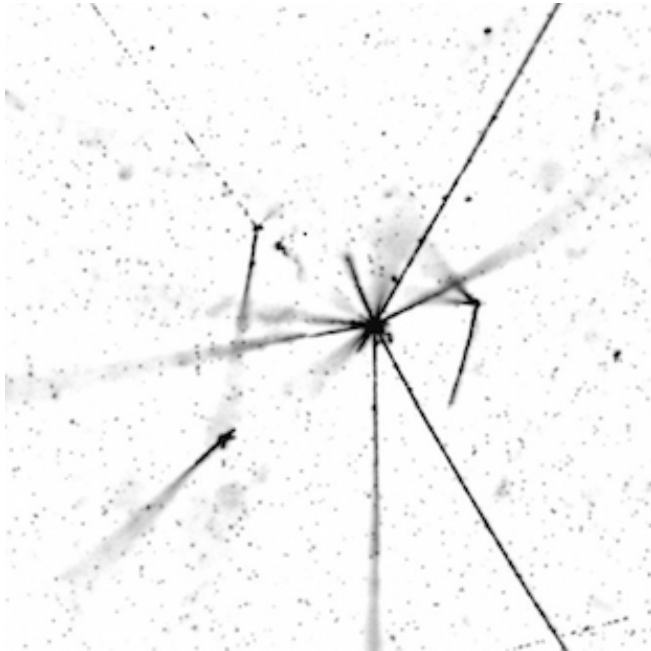
Another way to trace charged particles is by putting a fluid close to phase transition in their path. When the charged particle interacts with the liquid, it produces heat, letting the fluid change its phase, such that bubbles will form. Bubble chambers and cloud chambers use this effect to produce and image such traces. The length, thickness and shape of the trace is determinant for the particle generating it. To be able to reconstruct one event, several images from different angles are needed. Figure 2 is a good example of an interaction seen in such a detector.

Photoemulsion films

Using a specially chosen chemical compound, which alters its state permanently after interacting with incident radiation, offers a further possibility to trace charged particles. Photoemulsion films exploit this idea and lead to images like the one illustrated in figure 4. The grains become visible after a development process, revealing

Watch Professor Sumner Davis' Advanced Laboratory on Bubble Chambers

the tracks left behind by the particles. The OPERA experiment was able to proof the appearance of tauon neutrinos in a muon neutrino beam using this technique¹¹.



¹¹ Antonio Ereditato. The discovery of the appearance of $\nu_\mu \rightarrow \nu_\tau$ neutrino oscillations. *Nuclear Physics B*, 908: 116 – 129, 2016. ISSN 0550-3213. DOI: <http://dx.doi.org/10.1016/j.nuclphysb.2016.03.014>. URL <http://www.sciencedirect.com/science/article/pii/S055032131600105X>. Neutrino Oscillations: Celebrating the Nobel Prize in Physics 2015

Time projection chambers

In a medium the ionized atoms generated by the incident radiation recombine shortly after being ionized. By applying an electric field, recombination can be suppressed and the ionization electrons can be trapped, letting them drift through the fluid towards a charge collector. The path can be reconstructed if the drift speed is constant and the time the particle was drifting is determined. These kind of detectors are called time projection chambers (TPCs). MicroBooNE, SBND and Icarus feature liquid argon time projection chamber (LArTPC) in their apparati. A few events as registered by the LArTPCs of MicroBooNE are displayed in figure 5.

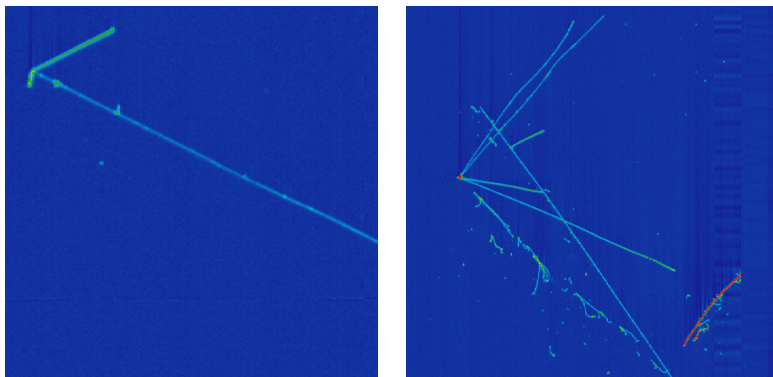


Figure 4: Interaction of an anti-proton with a nucleon of an atom in a photo-emulsion film. The AEgIS experiment – source of this event – uses such emulsion films to measure the gravitational force on antihydrogen – ©LHEP Universität Bern

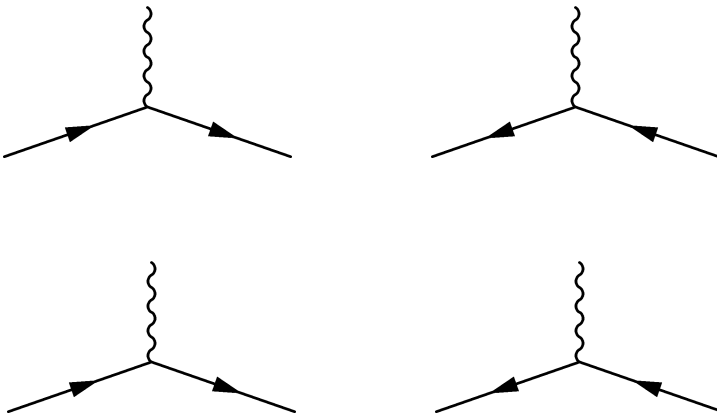
Figure 5: The event on the left is a candidate of a quasi-elastic scattering event. The event on the right is probably a deep inelastic scattering event with a candidate of a cosmic ray. – ©fnal.gov

Neutrino interactions

Neutrinos are studied by observing their interactions. It is therefore essential to know our model's neutrino interactions. This section aims to list the known neutrino interactions using Feynman diagrams, classify events into common energy ranges using the energy-momentum transfer and list the elastic and quasi-elastic scattering interactions of neutrinos and anti-neutrinos.

Currents of the weak interaction

Ignoring gravitational interactions, neutrinos are assumed to interact only under weak interactions. Consequently the involved mediators are the massive W^\pm - and the Z-boson, the mediators for charged currents (CCs) and neutral currents (NCs).



For interactions mediated by a NC the neutrino remains a neutrino and the anti-neutrino remains an anti-neutrino. When a neutrino interacts with another particle mediated by a CC the resulting particle is the neutrino's associated lepton. Anti-neutrinos consequently become their associated anti-lepton. Since the lepton and anti-lepton's charge differ, the currents – and therefore the mediators – need to differ as well. Figure 6 displays the Feynman diagrams of these two interactions.

A handy tool to describe particle interactions! Watch Feynman explaining their functionality in a lecture series at the University of Auckland in 1979.

Massive bosons: 80GeV and 91GeV. The high mass of the mediators is the reason for the short range of the weak interaction.

Figure 6: Feynman diagrams of (ftltbr) neutrino and anti-neutrino interacting with neutral and charged currents.

Due to conservation of charge.

Energy-momentum transfer and event classification

The interactions can be classified using the energy-momentum transfer between the interacting particles. Assuming we know the initial and final four-momenta of an interacting particle $p_i^\mu = (E_i, \vec{p}_i)$ and $p_f^\mu = (E_f, \vec{p}_f)$, then the momentum energy transfer is given by

$$q = p_i^\mu - p_f^\mu = (\Delta E, \Delta \vec{p}).$$

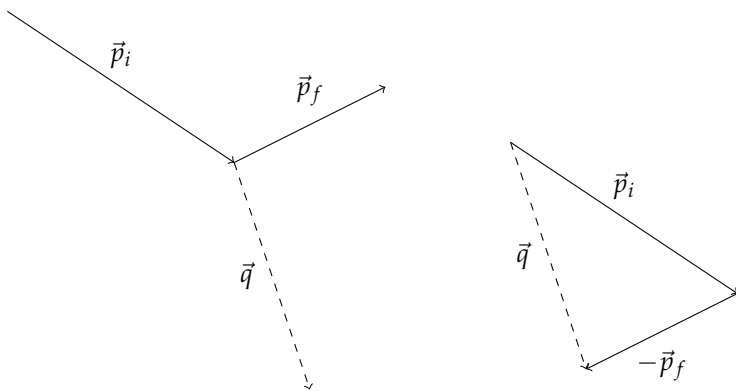


Figure 7: Illustration of the momentum transfer. \vec{p}_i and \vec{p}_f indicate the initial and final momenta. The image on the left shows the interaction of a classical particle transferring the momentum \vec{q} . If the momenta are rearranged like in the image on the right, it is obvious that \vec{q} is given by $\vec{p}_i - \vec{p}_f$.

Given a flat Minkowski-space, the square of the norm of q is given by

$$|q|^2 = (\Delta\vec{p})^2 - (\Delta E)^2,$$

where ΔE is the total transferred energy and $\Delta\vec{p}$ the total transferred momentum. We can define how massive an event is

$$\begin{aligned} Q^2 &= (\Delta E)^2 - (\Delta\vec{p})^2 \\ &= -q^2, \end{aligned}$$

and use this factor Q^2 to classify neutrino interaction events into:

Elastic & quasi-elastic scattering	$Q^2 < 1\text{GeV}^2$
Resonant scattering	$Q^2 \approx 1\text{GeV}^2$
Deep inelastic scattering	$Q^2 > 1\text{GeV}^2$

See the analogy to $m^2 = E^2 - p^2$?

Elastic & quasi-elastic scattering

Interactions of Q^2 below 1GeV^2 are called elastic scattering events if they were mediated by the NC. Low energy scattering events mediated by CC do not conserve kinetic energy, since part of it is needed to come up for the mass difference of the neutrino and its associated charged lepton. For this reason these events are called quasi-elastic. The terms charged current quasi elastic (CCQE) and neutral current elastic (NCE) are commonly used to refer to these two classes of events.

If we list all possible interactions of neutrinos and anti-neutrinos with matter and anti-matter, we can see, that there's a clear symmetry in the case of the NCE – see figure 8. The diagram for interactions of neutrinos with matter is equivalent to the diagram for the interactions of anti-neutrinos with anti-matter. The same occurs for interactions of neutrinos with anti-matter and anti-neutrinos with matter.

CCQE lack such a symmetry, i.e. none of the four diagrams is equivalent – see figure 9. Similar diagrams are found by changing the involved particles and mediators by their anti-particles and viceversa.

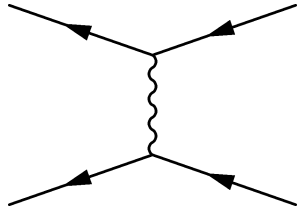
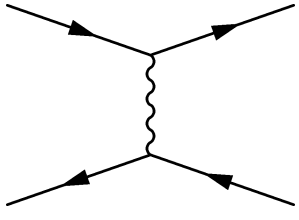
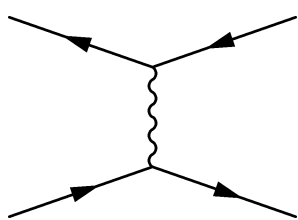
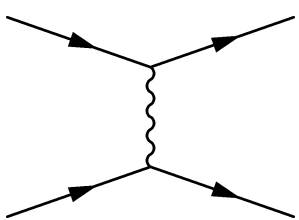
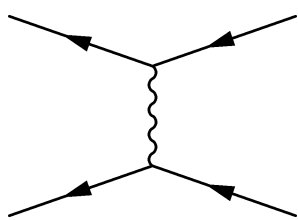
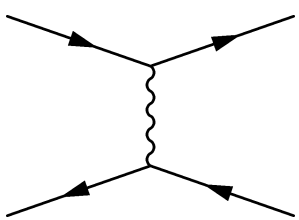
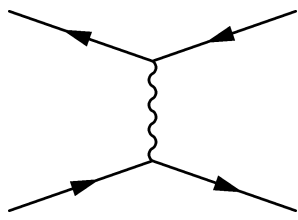
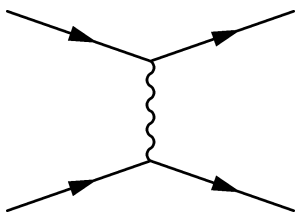


Figure 8: First order neutrino elastic scattering Feynman diagrams. q stands for a quark of any flavor in a baryon, since quarks are not found free in nature. The diagram on the top left is equivalent to the diagram on the bottom right. The diagrams on the top right and the bottom left are equivalent as well.

Figure 9: First order Feynman diagrams for quasielastic scattering. u and d stand for up-like and down-like quarks in a baryon. No equivalence can be found in these diagrams.

Neutrino sources

Neutrinos have a very small cross-section and interact very rarely. Many neutrinos emerge from natural and non natural sources adding an important signal background to any observation. It is important to quantify the background's value of any source whose neutrinos may interact in our detector and bias our observations. This section covers known natural and human induced neutrino sources.

... and matter is virtually transparent for them

Natural sources

Geoneutrinos are neutrino emitted in a β -decay of a radionuclide naturally occurring in the Earth. Most geoneutrinos are electron antineutrinos and originate from β^- -decay-branches of ^{40}K , ^{232}Th and ^{238}U . Referr to Geo-neutrinos¹² for a detailed review and analysis of the results from the KamLAND and Borexino data.

Atmospheric neutrinos result from the interaction of cosmic rays with an atomic nucleus in the Earth's atmosphere. These interactions generate showers of unstable particles – mostly pions (π) – whose decay involves the production of neutrinos. For more information on cosmic rays refer to section on background detection and mitigation.. The atmospheric neutrino flux is studied using the data of the IceCube experiment¹³ and Super-Kamiokande¹⁴.

Solar neutrinos The greatest neutrino background contribution is made by the sun. The main solar neutrino radiation comes from the proton-proton reaction, which is one of the known fusion reactions by which stars convert hydrogen to helium. Important contributions are made by the reactions of beryllium and boron. Solar neutrinos are best reviewed with the data of the Sudbury Neutrino Observatory¹⁵.

Other sources

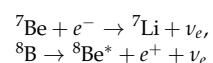
Reactor neutrinos Neutrinos emerging from interactions in nuclear reactors are called reactor neutrinos. The emission spectrum depends strongly on the type of nuclear reactions produced in the reactor.

¹² G. Bellini, A. Ianni, L. Ludhova, F. Mantovani, and W. F. McDonough. Geo-neutrinos. *Progress in Particle and Nuclear Physics*, 73:1–34, November 2013. DOI: [10.1016/j.ppnp.2013.07.001](https://doi.org/10.1016/j.ppnp.2013.07.001)

¹³ M. G. Aartsen et al. Observation and characterization of a cosmic muon neutrino flux from the northern hemisphere using six years of icecube data. 2016

¹⁴ E. Richard et al. Measurements of the atmospheric neutrino flux by super-kamiokande: energy spectra, geomagnetic effects, and solar modulation. 2015

86% of the solar neutrinos are produced by: $p + p \rightarrow d + e^+ + \nu_e$



¹⁵ A. Bellerive, J. R. Klein, A. B. McDonald, A. J. Noble, and A. W. P. Poon. The sudbury neutrino observatory. *Nucl. Phys.*, B908:30–51, 2016. DOI: [10.1016/j.nuclphysb.2016.04.035](https://doi.org/10.1016/j.nuclphysb.2016.04.035)

Nuclear scientific reactors, power-plants, nuclear submarines, etc.

So studying a reactor's neutrino spectrum allow to study nuclear power plants.

Neutrino beams When particles in rest decay by a two body decay, the energy and momenta of the resulting particles are known exactly. It is well known that the lightest charged mesons (π^\pm) decay into muons and their associated neutrinos, therefore the previous effect can be taken in advantage to build a neutrino beam out of decaying charged pions.

Neutrino oscillations and anomalies in the observations

Neutrino oscillations have been observed by numerous experiments, yet there's a discrepancy in the results of the different experiments. It is important to know how neutrino oscillations are modeled and the possible effects that alter our expected observations. This section includes simple oscillation models, matter effects and results from the neutrino oscillation experiments LSND and MiniBooNE.

Neutrino oscillation models

Neutrino oscillations are a consequence of flavour neutrino mixing in vacuum¹⁶. This can be modeled using a linear combination of the fields of the massive neutrinos ν_m for the flavor neutrino field ν_f in the charged current weak interaction

$$\nu_f = \sum_m U_{fm} \nu_m,$$

where $f \in \{e, \mu, \tau\}$ is the index for the flavor eigenstate and $m \in \{1, 2, 3\}$ is the index for the mass eigenstate.

U_{fm} is an unitary matrix generally called *mixing* matrix. The parametrization of this unitary matrix depends on the number of neutrino flavors and their characterization into *Majorana* or *Dirac* particles. Assuming there are n neutrino flavors and n massive neutrinos, the mixing matrix U can be parametrized by $\frac{n(n-1)}{2}$ Euler angles (see figure 10) and $\frac{n(n+1)}{2}$ phases in the case of Majorana neutrinos or $\frac{(n-1)(n-2)}{2}$ phases if neutrinos are Dirac particles¹⁷.

In the following 3 types of flavor field and mass field eigenstates are assumed. We impose furthermore, that none of the eigenstates is identical to another

$$\langle \nu_l' | \nu_l \rangle = \delta_{l'l}, \quad \langle \bar{\nu}_l' | \bar{\nu}_l \rangle = \delta_{l'l}, \quad \langle \bar{\nu}_l' | \nu_l \rangle = 0,$$

where $l \in \{e, \mu, \tau\}$ or $l \in \{1, 2, 3\}$.

In the case of Dirac massive neutrinos the representation of U is given the three angles $\theta_{12}, \theta_{13}, \theta_{23}$ and just one charge parity conjugation symmetry (CP) violation phase δ

$$\begin{aligned} U_D &= \begin{bmatrix} U_{e1} & U_{e2} & U_{e3} \\ U_{\mu 1} & U_{\mu 2} & U_{\mu 3} \\ U_{\tau 1} & U_{\tau 2} & U_{\tau 3} \end{bmatrix} \\ &= \begin{bmatrix} 1 & 0 & 0 \\ 0 & c_{23} & s_{23} \\ 0 & -s_{23} & c_{23} \end{bmatrix} \begin{bmatrix} c_{13} & 0 & s_{13} e^{-i\delta} \\ 0 & 1 & 0 \\ -s_{13} e^{i\delta} & 0 & c_{13} \end{bmatrix} \begin{bmatrix} c_{12} & s_{12} & 0 \\ -s_{12} & c_{12} & 0 \\ 0 & 0 & 1 \end{bmatrix} \\ &= \begin{bmatrix} c_{12} c_{13} & s_{12} c_{13} & s_{13} e^{-i\delta} \\ -s_{12} c_{23} - c_{12} s_{23} s_{13} e^{i\delta} & c_{12} c_{23} - s_{12} s_{23} s_{13} e^{i\delta} & s_{23} c_{13} \\ s_{12} s_{23} - c_{12} c_{23} s_{13} e^{i\delta} & -c_{12} s_{23} - s_{12} c_{23} s_{13} e^{i\delta} & c_{23} c_{13} \end{bmatrix}, \end{aligned}$$

where $c_{ij} = \cos(\theta_{ij})$ and $s_{ij} = \sin(\theta_{ij})$.

...or lepton mixing

¹⁶ K. A. Olive et al. Review of Particle Physics. *Chin. Phys. C* 38:090001, 2014.
doi: 10.1088/1674-1137/38/9/090001

...but also known as the Pontecorvo-Maki-Nakagawa-Sakata (PMNS) mixing matrix

Whilst Majorana particles are their own anti-particles, particle and anti-particle differ when dealing with Dirac particles.

¹⁷ Zhi-zhong Xing and Ye-Ling Zhou. Majorana CP-violating phases in neutrino-antineutrino oscillations and other lepton-number-violating processes. *Phys. Rev.*, D88:033002, 2013.
doi: 10.1103/PhysRevD.88.033002

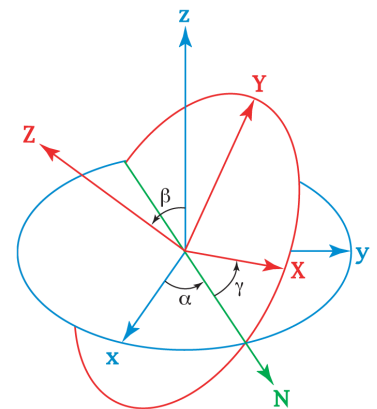


Figure 10: Illustration of the Euler angles between two rotated 3-dimensional reference frames. – ©wikimedia.org

If neutrinos are Majorana particles, two more CP phases are needed. These two phases can be taken into account by multiplying U_D with a diagonal matrix P containing the additional Majorana CP violation phases ρ and σ

$$\begin{aligned} U_M &= U_D P \\ &= \begin{bmatrix} U_{e1} & U_{e2} & U_{e3} \\ U_{\mu 1} & U_{\mu 2} & U_{\mu 3} \\ U_{\tau 1} & U_{\tau 2} & U_{\tau 3} \end{bmatrix} \begin{bmatrix} e^{i\rho} & 0 & 0 \\ 0 & e^{i\sigma} & 0 \\ 0 & 0 & 1 \end{bmatrix}. \end{aligned}$$

Two flavor oscillation probabilities in vacuum

The neutrino oscillation probability's complexity is reduced if assumed only two flavor eigenstates (ν_e, ν_μ) and two mass eigenstates (ν_1, ν_2). In that case the mixing matrix reduces to

$$\begin{aligned} U &= \begin{bmatrix} U_{e1} & U_{e2} \\ U_{\mu 1} & U_{\mu 2} \end{bmatrix} \\ &= \begin{bmatrix} \cos(\theta) & \sin(\theta) \\ -\sin(\theta) & \cos(\theta) \end{bmatrix}, \end{aligned}$$

With only 2 Dirac neutrinos, the number of euler angles reduce to 1 and no phases appear.

where θ is the euler angle. Consequently the flavor neutrinos can be written down in the form

$$\begin{aligned} |\nu_e\rangle &= \cos(\theta) |\nu_1\rangle + \sin(\theta) |\nu_2\rangle, \\ |\nu_\mu\rangle &= -\sin(\theta) |\nu_1\rangle + \cos(\theta) |\nu_2\rangle. \end{aligned}$$

Since the solutions of a plane wave can be used to describe the propagation of the mass eigenstates, we can state

$$|\nu_m(t)\rangle = e^{-i(E_m t - p_m x)} |\nu_m(0)\rangle,$$

where E_m and p_m are the energy and momentum of the m th eigenstate. The probability to find an electron neutrino in a beam of muon neutrinos is given by

$$\begin{aligned} P_{\nu_\mu \rightarrow \nu_e} &= |\langle \nu_e(t) | \nu_\mu \rangle|^2 \\ &= |\sin(\theta) \cos(\theta) (e^{-i(E_1 t - p_1 x)} - e^{-i(E_2 t - p_2 x)})|^2 \\ &= \sin^2(\theta) \cos^2(\theta) (2 - e^{-i\Delta E t} - e^{i\Delta E t}) \\ &= \frac{1}{2} \sin^2(2\theta) (1 + \cos(\Delta E t)) \\ &= \sin^2(2\theta) \sin^2\left(\frac{\Delta E t}{2}\right). \end{aligned}$$

The momentum of the particle is simplified to one dimension

Used identities:

$$\begin{aligned} \langle \nu_\mu | \nu_i \rangle &= \delta_{\mu i} \\ \Delta E &= E_1 - E_2 \\ p_1 &= p_2 \\ \sin^2(\varphi) \cos^2(\varphi) &= \frac{1}{4} \sin^2(2\varphi) \\ e^{i\varphi} &= \cos(\varphi) + i \sin(\varphi) \\ \cos(\varphi) &= \cos(-\varphi) \\ \sin(\varphi) &= -\sin(-\varphi) \\ 1 - \cos(2\varphi) &= 2 \sin^2(\varphi) \end{aligned}$$

Since neutrinos' mass is very small in comparison to their momentum, we can approximate their energy by the Taylor expansion around p_i and set $p_i \approx E_i \approx E$ getting

$$\begin{aligned} E_i &= \sqrt{p_i^2 + m_i^2} \\ &\approx p_i + \frac{m_i^2}{2E_i} \\ &\approx E + \frac{m_i^2}{2E}, \end{aligned}$$

to find

$$\begin{aligned}\Delta E &= \frac{m_1^2 - m_2^2}{2E} \\ &= \frac{\Delta m^2}{2E}.\end{aligned}$$

It's $\Delta(m^2)$ not $(\Delta m)^2$!

Setting $t \approx \frac{L}{c} = L$ – since neutrinos are always ultrarelativistic – leads to the well known formula for two flavor neutrino oscillations

$$P_{\nu_\mu \rightarrow \nu_e}(L) = \sin^2(2\theta) \sin^2(\Delta m^2 \frac{L}{4E})$$

Knowing the energy E of the muon neutrino flux and the distance L between the source of the muon neutrino flux and the detector the angle θ can be determined.

Matter effects

The occurring neutrino interactions depend on the type of matter and the neutrino flavor. Since condensed matter is composed mainly of neutrons, protons and electrons the possible interactions for muon and tauon neutrinos ν_μ, ν_τ reduce to the interactions with hadronic matter, while electron neutrinos ν_e interact with the electrons as well. Hence matter affects the passage of neutrinos of different flavors differently. This can be elucidated by taking a look at the Feynman diagrams for the neutrino interactions with matter.

... the Michejew-Smirnow-Wolfenstein effect

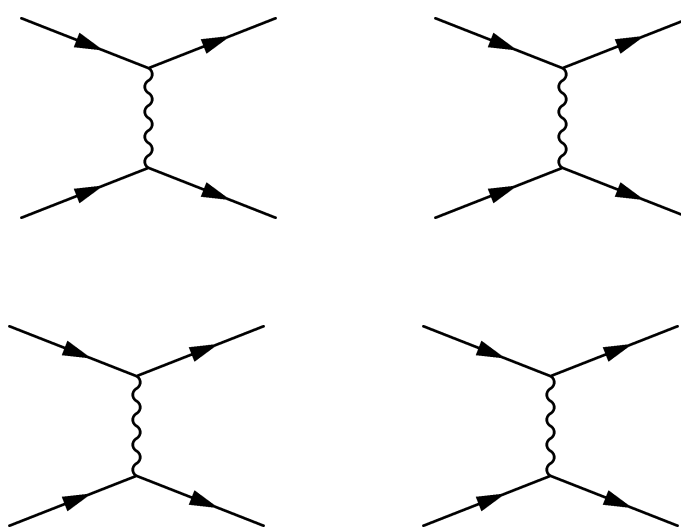


Figure 11: Interactions neutrinos with common matter.

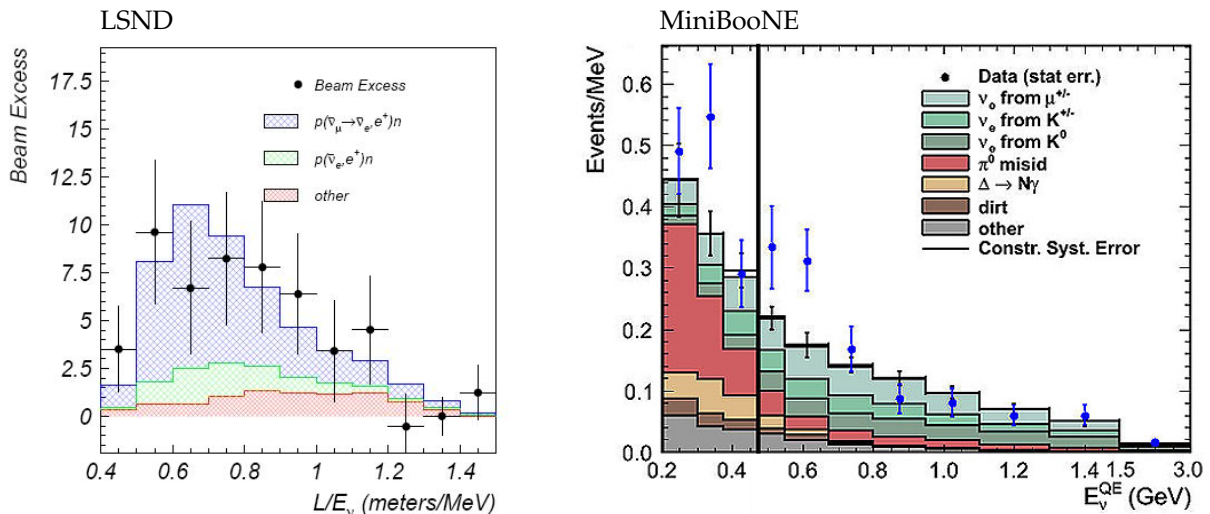
Since the coupling for all interactions is the same, it is clear that the event rate for electron neutrinos will differ from the event rate of tauon and muon neutrinos. This affects the oscillations of the neutrinos of different types and needs to be taken into account in neutrino oscillations.

Anomalies in neutrino oscillation observations

Liquid Scintillator Neutrino Detector

The LSND run from 1993 to 1998 to study neutrino oscillations at the Los Alamos Meson Physics Facility. The used Cherenkov detector contained 167t of mineral oil and was placed at only 30m distance from the target. Interactions of neutrinos with protons, electrons and atom nuclei were observed the from 20 to 200 MeV $\bar{\nu}_\mu$ -beam.

To see oscillations $\bar{\nu}_\mu \rightarrow \bar{\nu}_e$, the LSND-collaboration looked for electron antineutrino reactions. Due to the proximity of the detector to the target, the expected contribution of electron neutrinos was small. The observed rate was significantly higher than the expected value, such that it could not be explained with the common oscillation theory – see figure 12 for an illustration.



MiniBooNE

MiniBooNE was designed to observe neutrino oscillations and unambiguously verify or refute the LSND controversial result in a controlled environment. The MiniBooNE detector was a Cherenkov detector located 541 m away from the target and was based on mineral-oil.¹⁸ The detector contained 800t of ultrarefined mineral oil and methylene compounds as scintillating liquid. The experiment collected data for ten years from 2002 to 2012.

The results – see figure 12 – show an anomaly in the low energy distribution of the quasi-elastic neutrino events. The observation indicate an excess of low energy electron-like events in CCQE.¹⁹

Figure 12: The plot on the left shows the beam excess observed by LSND. The blue region represents the required oscillation from $\bar{\nu}_\mu \rightarrow \bar{\nu}_e$. The plot on the right displays the excess of events at low energies observed by MiniBooNE.

¹⁸ Teppei Katori and Janet Conrad. Beyond standard model searches in the miniboone experiment. *Adv. High Energy Phys.*, 2015:362971, 2015. DOI: 10.1155/2015/362971

¹⁹ S. N. Glinenko. The miniboone anomaly and heavy neutrino decay. *Phys. Rev. Lett.*, 103:241802, 2009. DOI: 10.1103/PhysRevLett.103.241802

Short Baseline Neutrino Program

Understanding the anomalies observed at LSND and MiniBooNE is one of the goals of the proposed SBN program. The program includes three LArTPCs located along the Booster Neutrino Beam (BNB) at Fermilab: Short-Baseline Near Detector (SBND), MicroBooNE and Icarus. This section aims to give an overview of the SBN program beam and detectors.

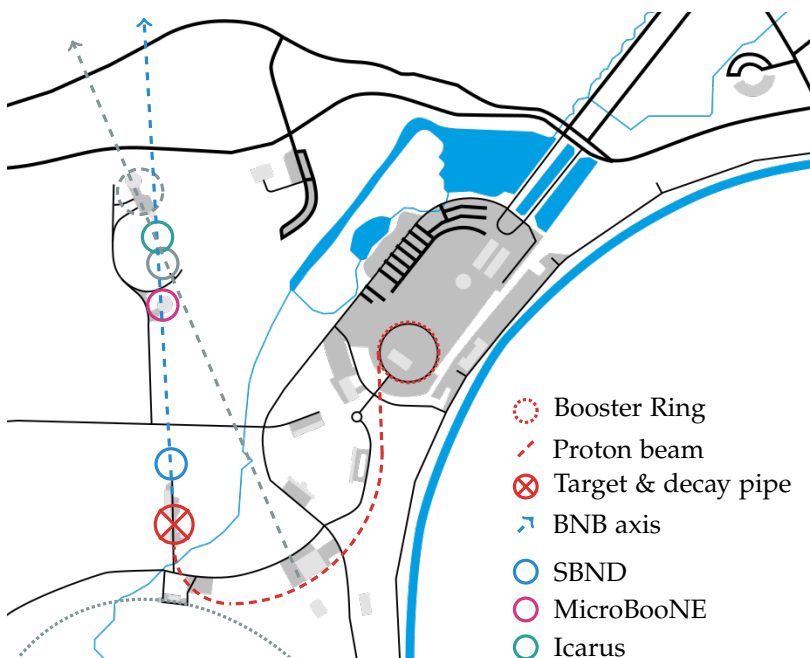
The Booster Neutrino Beam line

The BNB is one of the neutrino sources from Fermilab's Accelerator Complex, which comprises seven particle accelerators and storage rings. The BNB has successfully been operated for already 12 years in both neutrino and anti-neutrino modes. The fluxes are well understood, systematic uncertainties associated with the beam have also been determined²⁰. See figure 13 for an overview of the location of the accelerators, detectors and the BNB axis.

including the main injector, Neutrinos at the Main Injector (NuMI), the Tevatron, ...

²⁰ M. Antonello et al. A proposal for a three detector short-baseline neutrino oscillation program in the fermilab booster neutrino beam. 2015

Figure 13: Traced map of Fermilab and the detectors involved in the SBN program. The Main Injector, MiniBooNE, Minos, Minerva, Nova and the NuMI axis were added as reference points.



The beam's starting point is the radio-frequency quadrupole accelerator, which accelerates and separates the protons into bunches. Then the protons pass through a 150m linear accelerator before they're fed to the Booster Ring. After reaching energies of 8.89GeV in the ring the protons are guided to the beryllium target. The target measures 71cm long and is only 1cm in diameter. The resulting charged particles are focused using a magnetic horn and decay in a 50m long region filled with air, where the BNB is generated. This region can be shortened to 25m with the use of an absorber to influence the resulting flux.

The length of the target corresponds to 1.7 interaction lengths.

Commonly known as the decay pipe.

MicroBooNE

MicroBooNE is the first operative LArTPC detector of the SBN program. The observation of tracks started in August 2015 and the collaboration is already taking and registering data. Figure 5 displays some neutrino event candidates observed at MicroBooNE.

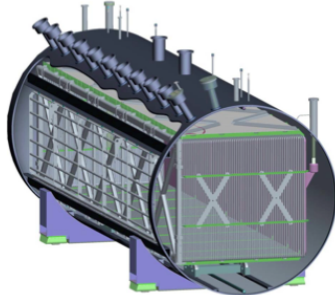


Figure 14: Scheme of the LArTPC of MicroBooNE

MicroBooNE's active mass is 89 tons and its LArTPC is contained in a cryostat. The active region is a rectangular volume of dimensions $2.33m \times 2.56m \times 10.37m$. The cathode is situated at the boundary of the active volume on the left beam side of the detector. The design of the chamber allows the ionization electrons of the charged particle tracks' to drift up to 2.56m to the wire grids, where the readout is made in the right beam side of the detector. Photon multiplier tubes (PMTs) are installed behind the read out wire planes to collect prompt scintillation light produced in the argon.

Short-Baseline Near Detector

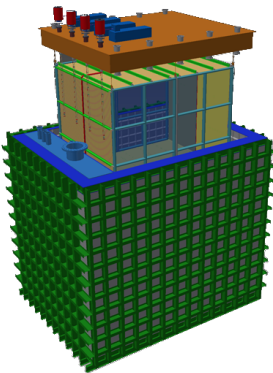


Figure 15: Scheme of the SBND

The SBND is a LArTPC in construction with an active volume of $4m \times 4m \times 5m$ at 110 meters from the BNB target – figure 15 illustrates its building concept. The LArTPC has a capacity for 112 tons of liquid argon and is contained in a membrane-style cryostat. It features four anode plane assemblies for signal readout. The maximal drift distance of the ionization electrons is 2m, $\approx 20\%$ shorter than the maximal drift length in MicroBooNE. SBND will additionally feature a light collection system for detecting the scintillation light produced in the argon volume. The operation of the SBND is planned to start in 2018.

Electron neutrino signals from cosmic background

A flux of particles from outer space constantly bombards the Earth's atmosphere, generating an important background signal in LArTPCs, the main reason for the construction of the CRT. This section handle cosmic rays (CRs) and the associated effects that contribute to neutrino signal..

Cosmic rays

Cosmic rays were discovered nearly a century ago and its origin and composition is not yet fully understood. The energy range of these incident particles is very wide, reaching ultra high energies above 10^8 GeV, whose origin is still unknown²¹. These cosmics travel millions of light years to before they reach earth, reason for which only stable particles are observed. Due to observed charges of these particles, the sources of these primary cosmic rays are assumed to be of electromagnetic nature.

²¹ M. T. Dova. Ultra-high energy cosmic rays. In *Proceedings, 7th CERN-Latin-American School of High-Energy Physics (CLASHEP2013): Arequipa, Peru, March 6-19, 2013*, pages 169–190, 2015. DOI: 10.5170/CERN-2015-001.169. URL <https://inspirehep.net/record/1452529/files/arXiv:1604.07584.pdf>

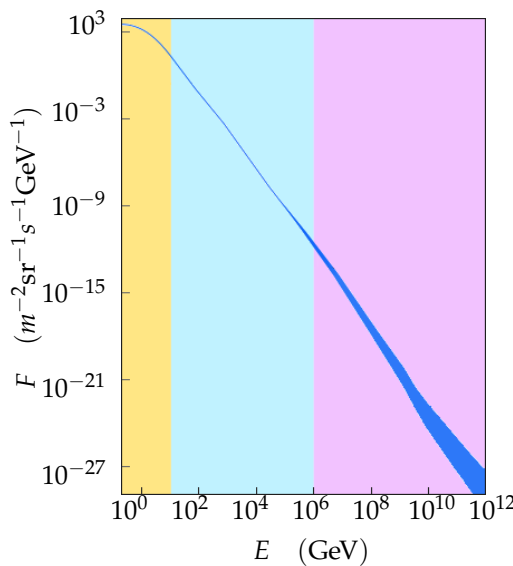


Figure 16: This plots displays the flux of cosmic rays in dependency of the particle's energy. The colored regions denote the particle fluxes: $1\text{m}^{-2}\text{s}^{-1}$ (yellow), $1\text{m}^{-2}\text{yr}^{-1}$ (cyan), $1\text{km}^{-2}\text{yr}^{-1}$ (magenta).

Using balloon-borne and space-based experiments the energy spectrum and components of CR have been studied²². The most abundant components of cosmic radiation are protons and helium nuclei. Elements of atomic number greater than Fe are extremely rare.

Cosmics contribute to the neutrino signal, due to the production of electromagnetic and hadronic showers of the constituents of the primary and subsequent cosmic rays. Electromagnetic showers involve many photons which can contribute to the neutrino signal. Hadronic showers result in neutral pions, which decay to high energy photons shortly after production.

²² Paolo Maestro. Cosmic rays: direct measurements. *PoS, ICRC2015:016*, 2015

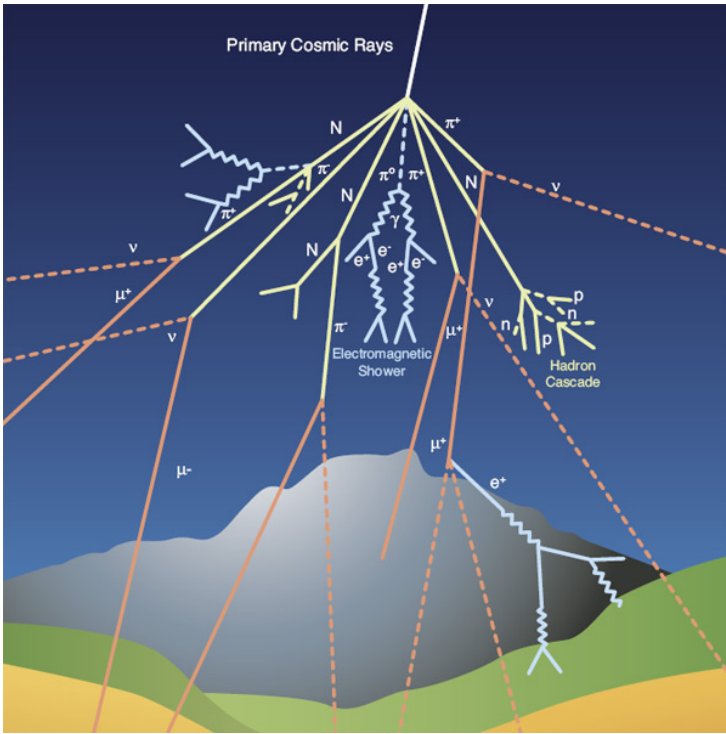


Figure 17: A primary cosmic ray interacts in the atmosphere and produces a shower of particles as illustrated.

Interactions contributing to the neutrino signal

Besides of the backgrounds contributed by the neutrino fluxes discussed in the section on neutrino sources, signal contributions of the high energy photons in these showers need to be taken into account.

The main contributions to the neutrino signal are given by Compton scattering events and electron positron production. Photons are not visible in the LArTPC's signal, the resulting free electrons from the photon interactions cannot be distinguished from a free electron of a neutrino interaction. See figure 18 for an illustration.

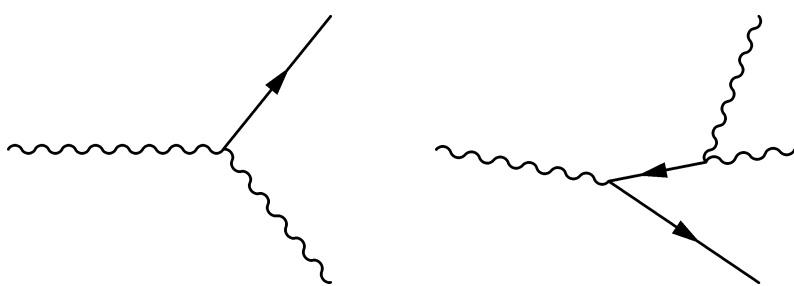


Figure 18: Compton scattering is displayed on the left. Pair production with subsequent annihilation of the positron with an electron of the medium is displayed on the right.

The contribution of Compton scattered electrons to the electron neutrino signal is comprehensible. In the case of electron-positron pair production, the subsequent annihilation of the positron with an electron in the medium is required, to interpret the event as a neutrino interaction.

The Cosmic Ray Tagger

Detecting and tracing incident ionizing background radiation to distinguish background from a BNB-based event in the LArTPC is the main goal of the CRT. This section covers the CRT modules functionality and important parameters are listed.

The Cosmic Ray Tagger in a nutshell

If the times and positions at which an incident particle entered and exited our detector are known, we can identify the crossing particle's trace. To trace incident radiation in a TPC, the latter needs to be covered with an additional detector generating a grid. This additional detector is the CRT and a scheme of it is illustrated in figure 19.

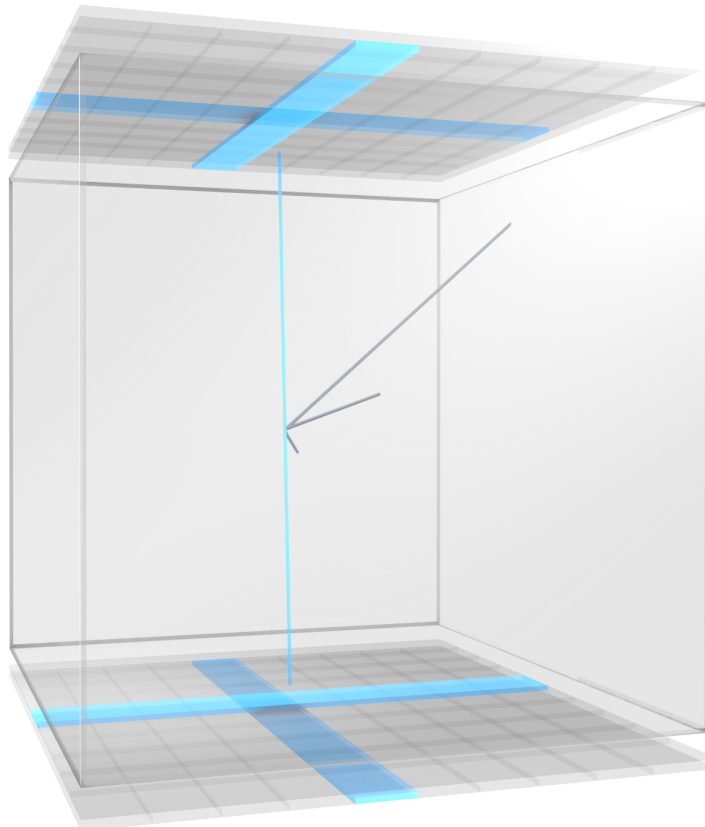


Figure 19: Schematic of two layers of CRT positioned above and below a virtual TPC containing an event. The event represents the interaction between a muon neutrino and a proton ($\nu_\mu + p \rightarrow p' + \pi^+ + \mu$) with an atmospheric muon travelling close to the event's vertex. The highlighted scintillating bars are crossed by the atmospheric muon. Using the grid produced by the scintillating bars the atmospheric muon's path can be identified.

The CRT consists of several independent detectors (modules), making it fully modulable. Each CRT module consists of a CRT panel and a Front-End Board (FEB), which processes the panel's incoming signals to event data. A layer of CRT requires at least two panels – to generate a grid of scintillating pixels – and two layers are needed to track incident particles. If the position of the panels is well known, their signals and time coincidence can be used to determine the entry and exit points of the incident particle.

Background mitigation

Charged particles will generate a signal in our CRT modules. Using these signals, a cylindrical volume can be constructed around the path of the incident particles. This volume acts as a veto for the track.

If the vertex of a neutrino event is inside the veto region, the event needs to be reconstructed with more delicate algorithms to distinguish the neutrino signal from the cosmic signal. The following parameters of the detector are of severe importance to achieve a useful veto signal with the smallest possible volume..

Time resolution The time a particle takes to cross our detector is given by the particle's velocity. If the CRT modules are run without using the coincidence signals featured by the FEB, these coincidences need to be reconstructed from the detector data. A precise time resolution is required for this task.

Position resolution is principally given by the width of the bars installed in the module. This resolution can be improved by calibrating the signal ratio and signal amplitudes for the channels of a bar.

Detection efficiency Not every occurrent particle transition is registered as an event by our detector. Many physical effects influence the particle detection efficiency of the CRT. An important contribution to detection efficiency is made by the set threshold, since it will change the part of the energy spectrum observed by the CRT.

Quantum efficiencies, geometrical fill factors, surface reflections, detection ranges, signal losses...

The Cosmic Ray Tagger panel

This section covers technical aspects of the panels' components as well as manufacturing processes.

The panel in a nutshell

A panel consists of 16 scintillating bars embedded in an aluminium cover. Each of the bars is prepared with two grooves, two wavelength shifting fiber (WLSF), a plastic endpiece and an electronics board with two embedded SiPM. See figure 20 for assembled and exploded assembly drawings of the scintillating bar.

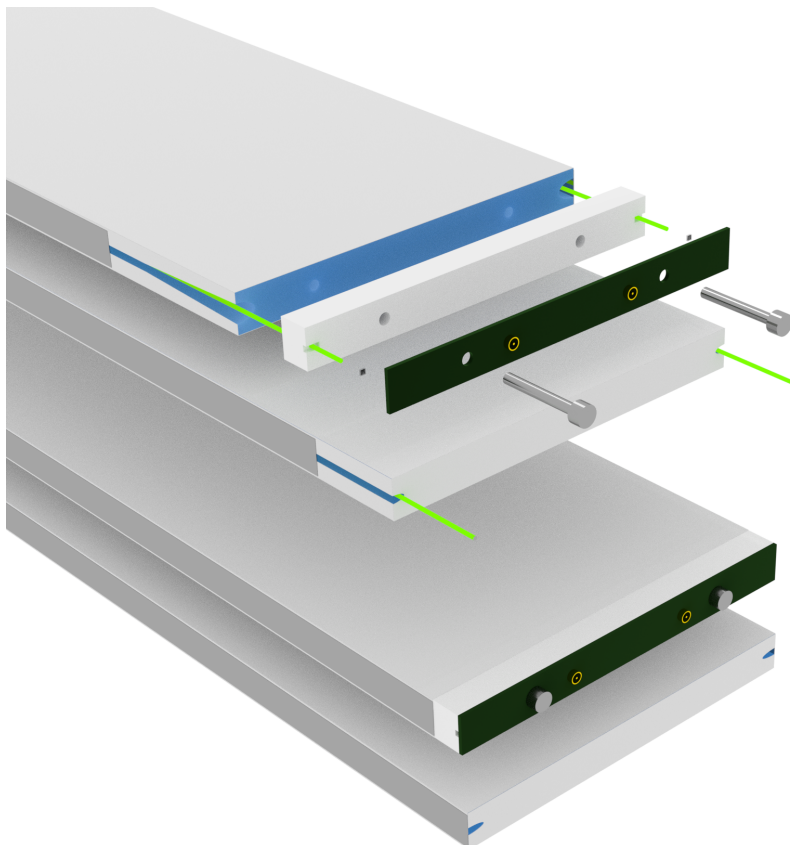


Figure 20: Assembled and exploded views of front and rear ends of scintillating bars. The long sides of the bars (blue) are furnished with grooves containing the WLSFs (fluorescent green) to guide the scintillation light to the SiPMs (black). The grooves are covered with mylar foil (gray). The plastic endpiece (white) serves as a physical guide and holder for the WLSFs. The electronics and the enpiece are fixed to the bar with screws. Optical glue keep the WLSFs and the mylar foil in place.

When a high energy particle traverses the panel, it will most likely cross one of the scintillating bars and induce the isotropical emission of photons. These photons will be attenuated along their path in the material and reflected on the bars' walls until some of them reach the WLSF. The WLSF are used for their light propagation properties and low attenuation coefficient, which allow some of the fluorescense photons to reach the SiPMs. The photons arriving to the SiPM may induce the discharge of a cell in the SiPM, generating an observable signal.

This likelihood depends on the fill factor of the panel

Aluminium shielding

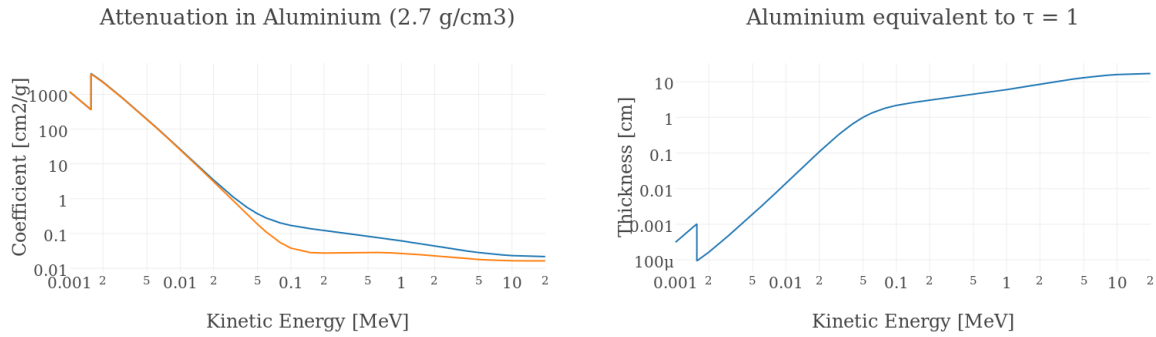
The bars are covered with sheets of aluminium to shield the scintillating plastic and SiPMs from photons and charged particles. The aluminium cannot dissipate all particle's energy, letting some photons and high energy particles through. Knowing the kind of radiation trespassing the detector is insightful, this is discussed for photons and charged particles.

Photons are attenuated exponentially by the material along their path

$$I(x) = I_0 e^{-\mu x},$$

where I_0 is the intensity of the transmitted radiation at the interface and x the perpendicular distance from the interface.

The attenuation depends on the energy of the photons, the nuclear structure and density of the material. The attenuation coefficients for aluminium are displayed in figure 21.



Since single photons can reach great depths in any material, it is more commonly used to express the thickness of a layer of material for incident radiation in optical depth

$$\tau = \mu x,$$

where μ is the attenuation coefficient and x the thickness of the layer of material.

Charged particles For charged particles the penetration range can be estimated using a continuously slowing down approximation and the stopping powers of aluminium for every kind of particle

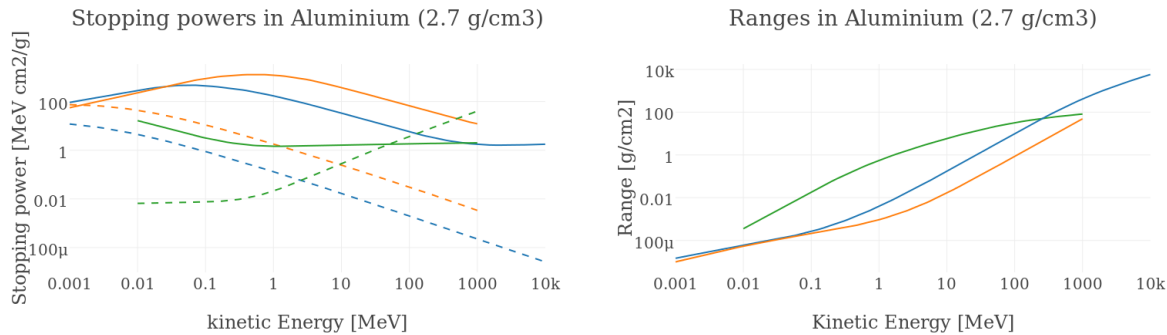
$$\begin{aligned} R(E_0) &= \int_{E_0}^0 \frac{1}{S(E)} dE \\ &= \int_{E_0}^0 -\frac{dx}{dE} dE. \end{aligned}$$

The high stopping power of aluminium for charged hadronic radiation stops heavy charged particles. The nuclear contribution to energy loss for charged hadronic radiation is negligible. Electrons lose almost all their kinetic energy to other electrons. The radiation

Figure 21: The plot on the left displays the attenuation coefficient (blue) and energy absorption coefficient (orange) for photons in aluminium. The right plot displays the thickness of aluminium required to have an optical depth of one. Data used from NIST tables. Data source: NIST Xray Mass Coefficients,

Assuming photons of the energy of 1.5 MeV – which is approximately the energy of the γ photons resulting from ^{40}K undergoing electron capture in ambient radiation – the mass attenuation coefficient of aluminium is $\mu_\rho = 0.05 \text{ cm}^2 \text{ g}^{-1}$ and therefore $\mu = \mu_\rho \rho = 0.135 \text{ cm}^{-1}$. The optical depth of $\tau = 1$ is reached with a $x = \frac{1}{\mu} = 7.4 \text{ cm}$ thick layer of aluminium. For photons of energies above 0.1 MeV, 2 mm of aluminium is almost transparent.

contributions of electrons start to be significant only for kinetic energies above 50MeV. Using the stopping powers the ranges inside aluminium in dependence of their energy can be computed. See figure 22 for an illustration of the stopping powers and ranges for electrons, protons and alpha particles in aluminium.



Scintillating bars

The scintillating bars generate the grid of the CRT and yields light from the incident radiation. A scintillator is a material which emits light through luminescence when exposed to radiation. When struck by ionizing radiation, a scintillator will absorb some of the radiation's energy and release the absorbed energy by light emission.

The scintillation light originates from an organic fluor which is mixed into the plastic out of which the bars are produced. The fluor excites into a metastable state, but its decay time is short, leading to almost no delay on the emission of the scintillation light. The scintillation light is emitted isotropically from the radiation's incident point. The components of the scintillating plastic are listed on table 1, the spectra of absorption and fluorescence of the scintillating components are displayed in figure 23.

Ingredient	Synonym	% WT
Styrolution PS GPPS		98.46
1,4-Diphenylbenzene	p-Terphenyl	1.5
1,4-Bis(5-phenyl-2-oxazolyl)benzene	POPOP	0.04

The bars come prepared with a thermal treatment, which increases the reflexion of light. The size of the bars vary, depending on the dimensions of the module they are built in. One side of the bars is faced to have a clean interface to fix the plastic endpiece to. The grooves need to be cut open before glueing the WLSF into them.

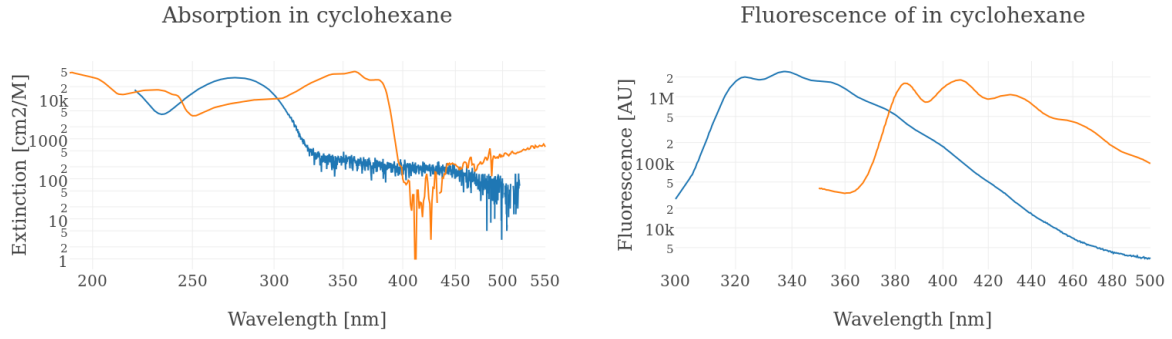
The scintillating bars are fixed to the aluminium sheets using double sided scotch tape. The short sides of the panels are fixed to a prepared aluminium bar with screws. The long sides of the panels are closed with U-shaped aluminium profiles, which are

Figure 22: The stopping powers (left) and continuously slowing down approximation (CSDA) ranges (right) are displayed for electrons (green), protons (blue) and alpha particles (orange). The radiative energy losses for the electrons and nuclear contributions for the hadros are dashed. Data source: NIST ESTAR, NIST PSTAR & NIST ASTAR

Luc Beaulieu gave a good review on Plastic Scintillation Detectors at the AAPM 2013.

The decay time is of the order of nano seconds.

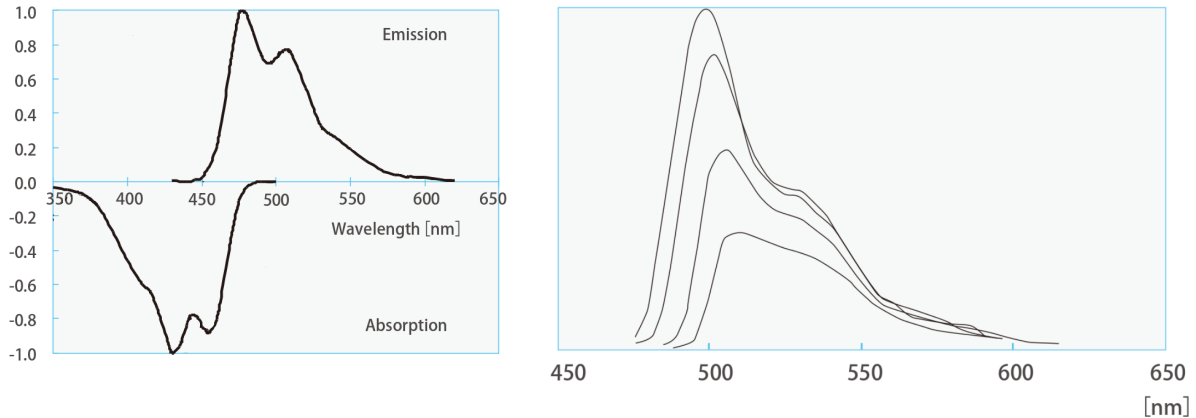
Table 1: Composition / Information on ingredients of the scintillating plastic used for the bars of the CRT.



fixed with glue to the rest of the panel. The gaps that might arise are closed with glue to minimize the transition of photons.

Wavelength shifting fibers

Since light is collected through the fiber's cladding and a very low attenuation coefficient is needed, a WLSF is used to guide the light from the scintillating bar to SiPMs. WLSF are very efficient light guides, since their emission and absorption spectrum is shifted, which leads to a very low attenuation coefficient. The absorption and emission spectrum and the attenuation of the spectrum along a fiber are displayed on figure 24. Further technical details for the WLSF Y-11 can be found on kuraray's website and its product catalogue.



The fibers are cut according to the length of the bars. Both ends of the fibers are faced using a diamond-cutter to optimize the interface. Aluminium is evaporated on the far end, to improve the reflexion of light. The uncoated end is put on top of the SiPM, by using the plastic endpiece as physical guide and holder. The fibers are glued to the groove using optical glue.

Figure 23: (fttb) Optical absorption and fluorescence emission spectrum of p-Terphenyl (blue) and POPOP (orange) in cyclohexane. Data from PhotochemCAD package, version 2.1a (Du 1998, Dixon 2005), <http://omlc.org/spectra/PhotochemCAD/>

Figure 24: Absorption and emission spectrum of the WLSFs displayed on the left shows peaking fluorescence emission at 476 nm and a maximal absorption at 430 nm. Attenuation of the spectrum of the WLSFs on the right displays the spectrum at different distances (fttb 10, 30, 100, 300cm) from the source's incident point. The used light source to excite the fibers had a wave length of 430nm. Source: kuraray's product catalogue

Silicon photomultiplier

A SiPM is an array of cells made of silicon, a well known semiconductor which is able to carry electrons and electron holes. Each cell of the SiPM behaves like a diode, the electronic equivalent of a SiPM is displayed in figure 25.

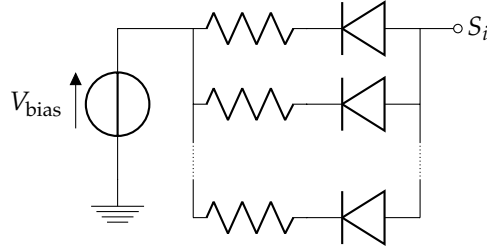
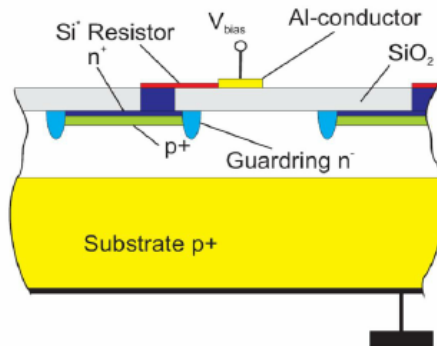


Figure 25: Each branch of this electronic scheme represents a cell of the SiPM. All cells of the same crystal share the same bias voltage.

The charge carriers in the cells' silicon lattice can be knocked out by incoming photons and drift to their appropriated electrodes if a field is applied. With greater field the drift velocity increases, to the point where further charged carriers are knocked out. With a sufficiently high voltage a photo electron leads to a self-sustaining avalanche. A typical structure of a cell is shown in figure 26.



also called breakdown voltage

Figure 26: Typical structure of a SiPM's cell. The cells are generally arranged on a 2 dimensional array. – ©M. Teshima, SiPM Development for Astroparticle Physics Applications

SiPMs are run in Geiger mode, in which each cell behaves like a capacitance. The amount of collected charge depends on the voltage applied to the SiPM's cells. Since the capacitances and the voltages are similar in within a SiPM, the collected charge is linearly proportional to the number of simultaneously discharged cells. The SiPMs used in the CRT are multi-pixel photon counters (MPPCs) produced by Hamamatsu. More data can be found on table 2.

and therefore linearly proportional to the number of incoming photons!

Parameter	Value
Effective photosensitive area	$1.3 \times 1.3 mm^2$
Number of cells	667
Geometrical fill factor	62%
Breakdown voltage	65V
Gain	$10^5 - 10^6$

Table 2: Product specifications for Hamamatsu MPPC S12825-050. Source: Hamamatsu Product Flyer

The Cosmic Ray Tracker Front-End Board

The Front-End Board FEB is designed to serve a CRT panel and process its signals to event data. The FEB is illustrated in figure 27. This section aims to explain the FEB's functionalities and list some of its features. For more detailed information please refer to the FEB's technical description²³.

The Front-End Board in a nutshell

The FEB completes a CRT module by supplying the SiPMs with a bias voltage and read out their signals. The FEB features a configurable bias voltage and threshold as well as a triggering logic to reduce background signal. The bias voltage is used to tune the gain of every SiPM while the threshold is used to discriminate events below a certain signal. Several FEBs can be set in coincidence, triggering events only if all the FEBs put in coincidence trigger an event in a short time window. This allows to arrange more complex setups. When several FEBs are used, they can be daisy-chained to send data via network to a single host.

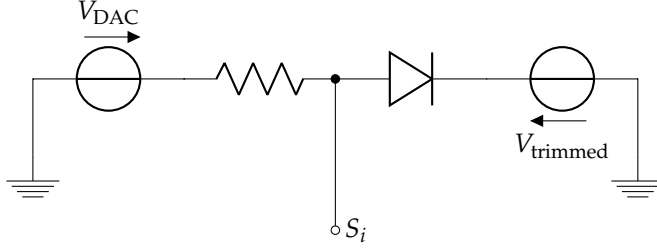
²³ M. Auger, A. Ereditato, D. Goeldi, I. Kreslo, D. Lorca, M. Luethi, C. Rudolf von Rohr, J. Sinclair, and M. S. Weber. Multi-channel front-end board for sipm readout. 2016



Figure 27: This figure shows the ports of the FEB (top) and the connector for the CRT panel (bottom). The ports are (fltr): TIN, TOUT for external coincidence signals, T₂, T₁ for time reference signals, power connector, 2x fast ethernet. The electronic components' board is visible from outside (green).

Bias voltage generator

Bias voltage is given by two opposed voltages: A stabilized power supply and the voltage output of a digital to analog converter (DAC). The voltage of the power supply is adjustable in a range from 50V to 90V by varying manually a trimmer resistor and is common for all 32 SiPMs served by the FEB. Individual adjustments for every channel are made using the output the DAC supplied on board. See figure 28 for a simplified scheme of the electronic circuit.



Triggering logic

One of the FEB's features is to trigger events only when both SiPMs of the same scintillating bar present simultaneously a sufficiently high signal. The signal S_i – for the i th SiPM – is amplified and shaped with a RC-CR-shaper. If the shaped signal is greater than the set threshold, the output of the discriminator T_i is positive. This output is combined with the corresponding signal of the associated SiPM, generating the pair trigger signal P_i . If one of the pairs trigger a signal is positive, the central processing unit (CPU) starts digitization of the event. Amplification, shaping and discrimination is done by CITIROC ASIC and signal logic is processed by a SPARTAN-6 field programmable gate array (FPGA). See figure 29 for an illustration of the electronic circuit.

Figure 28: The bias voltage is generated using a voltage source trimmed by a resistor. Voltage fine tuning for every channel is made with a configurable DAC's output. The DAC's constant output corresponds to a DC-offset of the signal lines, the DAC's full range is from +0.5V to +4.5V. Since the DAC's output is positive, increasing its value actually reduces the effective bias voltage for the SiPM. The SiPM is depicted as a single diode in this scheme for simplicity.

This coincidence requirement reduces the number of events caused by incident gamma radiation significantly.

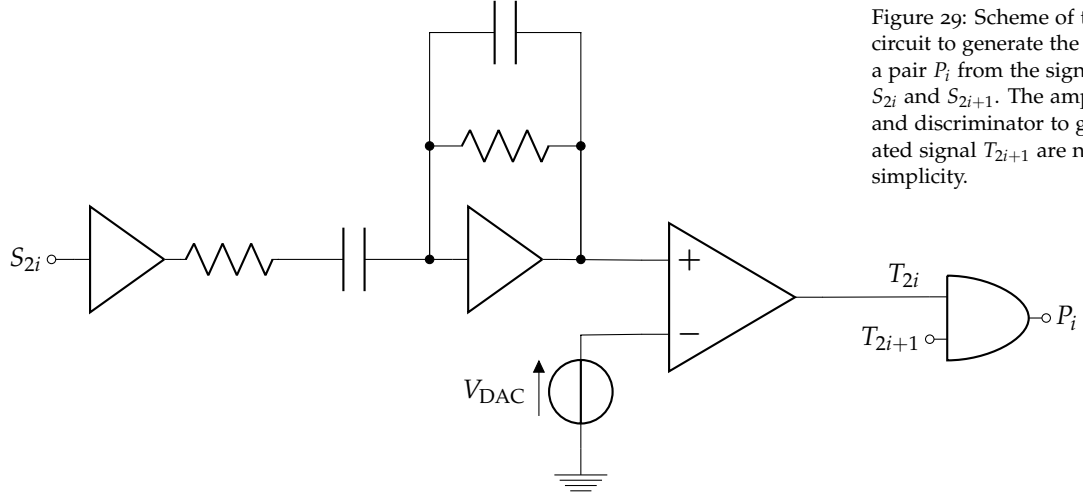


Figure 29: Scheme of the electronic circuit to generate the trigger signal for a pair P_i from the signals of two SiPMs S_{2i} and S_{2i+1} . The amplifier, shaper and discriminator to generate associated signal T_{2i+1} are not displayed for simplicity.

Analog signal readout and digitization

The FEB starts signal readout when an event trigger signal is triggered. In that case the signal of the SiPMs is amplified, shaped using a slow RC-CR shaper and stored in a sample-and-hold circuit. The stored analog signals are then digitized one by one using a 12-bit analog to digital converter (ADC) and an analog multiplexer, to switch between the signals to digitalize. Figure 30 illustrates the electronic circuit.

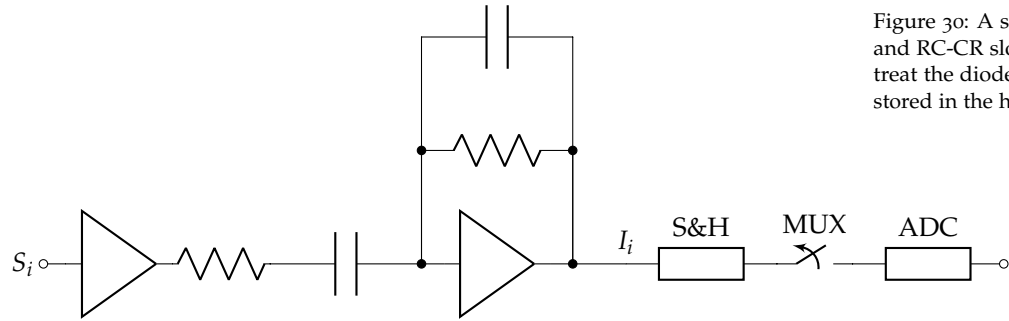


Figure 30: A series of amplifiers and RC-CR slow shapers are used to treat the diode's signal before being stored in the hold circuit.

Event data structure & storage

When an event is triggered and as soon as the ADC process is completed for all 32 channels, the result is combined with the time stamp to a packet of the following structure:

```
typedef struct {
    uint32_t flags;
    uint32_t T1;
    uint32_t T2;
    uint16_t adc[32];
} FEBEVT_t;
```

These event packets are stored in the internal ring buffer. Once the capacity of 1024 events is reached, new events will override present ones. The number of overwritten events is passed in the flags of the event packet.

The Front-End Board software

febdrv communicates with FEB and sends commands to it. *febdrv* allows to switch bias, data adquisition and configure the FEB. It also publishes statistics and stati of the connected FEBs and their observed event packets.

febctl sends commands to the *febdrv* to start and stop data acquisition (DAQ) and switch the FEB's bias voltage.

febconf reads configurations from files and sends them to the *febdrv* to change the FEB's settings.

febmon displays current status of the FEB published by *febdrv*.

Calibration of a Cosmic Ray Tagger module

While time resolution of the CRT can be calibrated without directly knowing the gain, calibrating the latter is critical for position resolution and efficiency of a CRT module. Given a fixed threshold, the efficiency of a SiPM depends strongly on the gain. This section introduces the distributions of the signals observed by the CRT module, the distribution's associated parameters, gain determination and calibration.

The signal spectrum

The event data obtained from febdrv is collected and the signal values are counted for every SiPM, leading to each SiPM's spectrum and the pedestal. The resulting distributions for the pedestal vary in dependence of the observed SiPM, therefore a sample spectrum is displayed in figure 31.

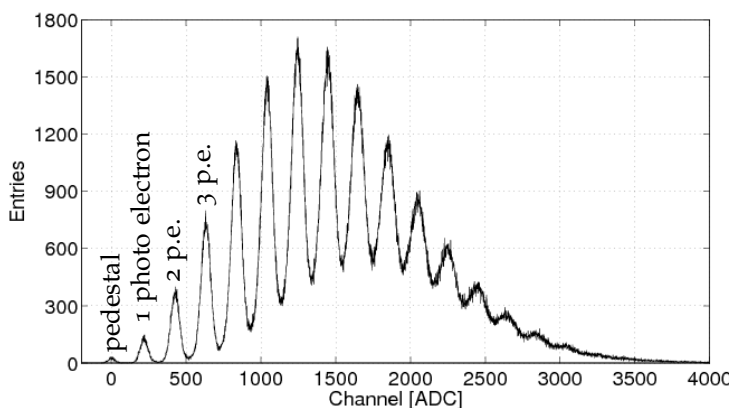


Figure 31: Sample spectrum of a SiPM. The first peak corresponds to the pedestal, followed by a series of peaks, each representing a number of simultaneously discharged cells. Since the uncertainties of the cells add up, the peaks get wider with increasing number of simultaneously discharged cells.

The spectrum of a SiPM consists of a series of peaks, the first peak corresponds to the pedestal, a gaussian distribution around the zero value. The nature of this pedestal is the electronic noise and the current leaks generated by the electronic components. The subsequent peaks correspond to simultaneously discharged SiPM cells and therefore to a number of photo electrons. Since every peak corresponds to a number of simultaneously discharged cells, the distances between the position of the peaks corresponds to the gain of the SiPM.

Signal & single photon resolution The signal in the readout is the sum of the signal when no avalanche occurs – also called pedestal – and the avalanche signal

$$S_i = S_{\text{pedestal}} + i \cdot G,$$

where G is the gain of signal in a SiPM and i is the number of photo electrons or simultaneously discharged cells.

The fluctuations of the pedestal and gain uncertainties determine the single photon resolution:

$$\sigma(i)^2 = \sigma_{\text{pedestal}}^2 + i \cdot \sigma_{\text{gain}}^2,$$

where i is the number of activated cells. The fluctuations in the pedestal originate from unpredictable current leaks and readout electronics noise. The uncertainties in the gains come from varying quenching resistances from cell to cell and the fluctuations during avalanche processes.

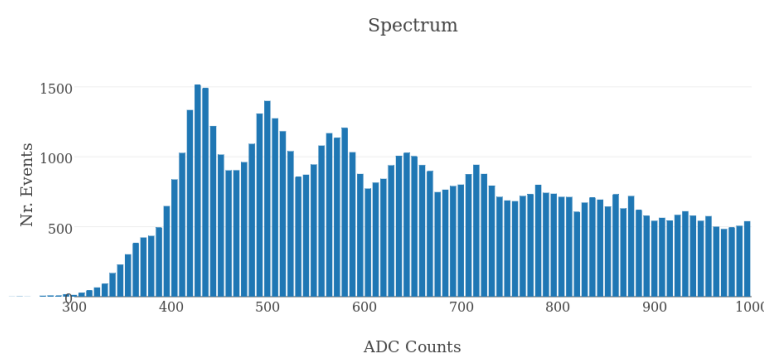
Dark rate, cross-talk & after pulses The dark rate is the event rate from avalanches generated by thermal or field mediated excitations of electrons in the silicon lattice and two correlated avalanche triggers: cross-talk and after pulses.

When the bias voltage is greater than the breakdown voltage, a charged carrier crossing the cell's p-n junction, can create a photon with sufficient energy to create an electron-hole pair. The probability of this happening is of the order of 10^{-5} , therefore for gains of the order of 10^5 , the number of these photons becomes significant²⁴. It is important to point out, that these photons can propagate into nearby cells and initiate an avalanche. This effect is called optical cross-talk.

During avalanches, electrons can be trapped in the Si-lattice and released later, producing a second avalanche after a characteristic time delay. These avalanches are generally called after pulses.

Determine the gain of a silicon photomultiplier

Since the distance between neighboring peaks allows to compute the gain of the SiPMs, a method to identify the peaks, determine their positions and compute the distances is needed. For this the part of the spectrum where the peaks are best visible is cut out.



First the positions of the peaks are estimated, using ROOT²⁵ and its TSpectrum class²⁶. Three search parameters are used to find estimates: the width of the peaks, the bin size and the threshold. Estimations are made by varying these parameters, each set of parameters leads to a search result with a number of peak candidates.

²⁴ Patrick Eckert, Rainer Stamen, and Hans-Christian Schultz-Coulon. Study of the response and photon-counting resolution of silicon photomultipliers using a generic simulation framework. 2012. DOI: 10.1088/1748-0221/7/08/Po8011

Figure 32: A small region of the spectrum has peaks, which are easy to identify.

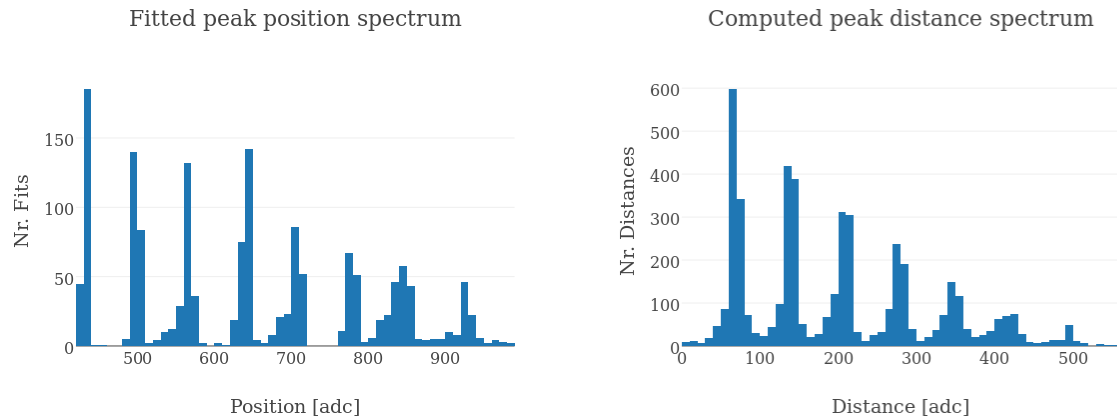
²⁵ Root data analysis framework. <https://root.cern.ch>. Accessed: 2016-09-09

²⁶ TSpectrum class reference. <https://root.cern.ch/doc/master/classTSpectrum.html>. Accessed: 2016-09-09

If the number of the estimated peak candidates is sufficiently high, but doesn't exceed the number of expected peaks, a gaussian distribution is found to fit each peak candidate. The resulting parameters are kept if the relative uncertainty of the position and the width is small. Every set of search parameters leads therefore to a number of fitted peaks. The fitted positions are counted in a histogram, displayed in figure 33.

$$\sigma < 5\%$$

... including fake peaks and missing some peaks sometimes!



Since not only real peaks but fake peaks are identified and fitted as peaks, taking the mean and the standard deviation of the distances leads to undesired results. This is avoided by computing the distances between the peaks for every set of fitted peaks. Putting all these distances in a histogram – as displayed in figure 33 – shows a series of clear features with decreasing height. Assuming the number of found fake peaks is low, the most occurring distance is the distance between two neighboring peaks. The position and width of a gaussian fitted around the greatest peak corresponds to the SiPM's nominal gain and its uncertainty in ADC counts per photo electron – see figure 34.

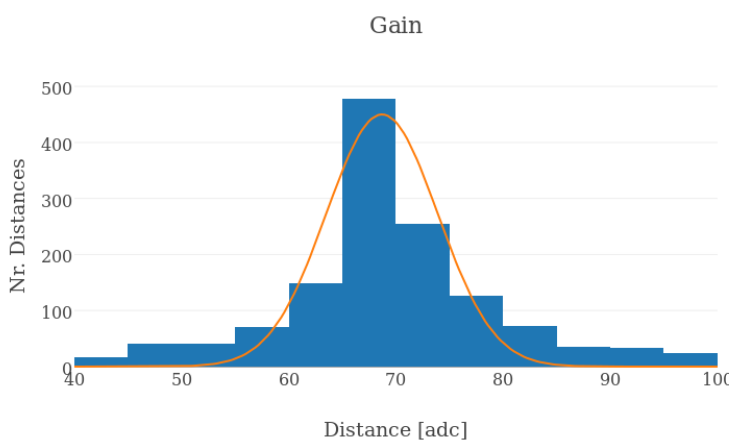


Figure 34: The plot displays the part of the histogram with the greatest peak and the fitted gaussian distribution around it.

Figure 33: The plot on the left shows the peak positions found for the given spectrum and different search parameters. The occurrences between the maxima show, that the search and fit method finds and registers fake peaks as well. The plot on the right displays the computed spectrum of distances. The first peak is the distance between two neighboring peaks. The second peak is the distance to the next proximate peaks, etc.

Dependency of the gain on the bias voltage

When driven in Geiger mode, the cell of a SiPM behaves like a capacitance, accumulating charge – which is responsible for the signal's gain – due to a voltage supplied by the FEB charge

$$G = \frac{C_{\text{cell}}}{e} (V_{\text{bias}} - V_{\text{breakdown}}) \quad (1)$$

$$= \frac{C_{\text{cell}}}{e} V_{\text{over voltage}} \quad (2)$$

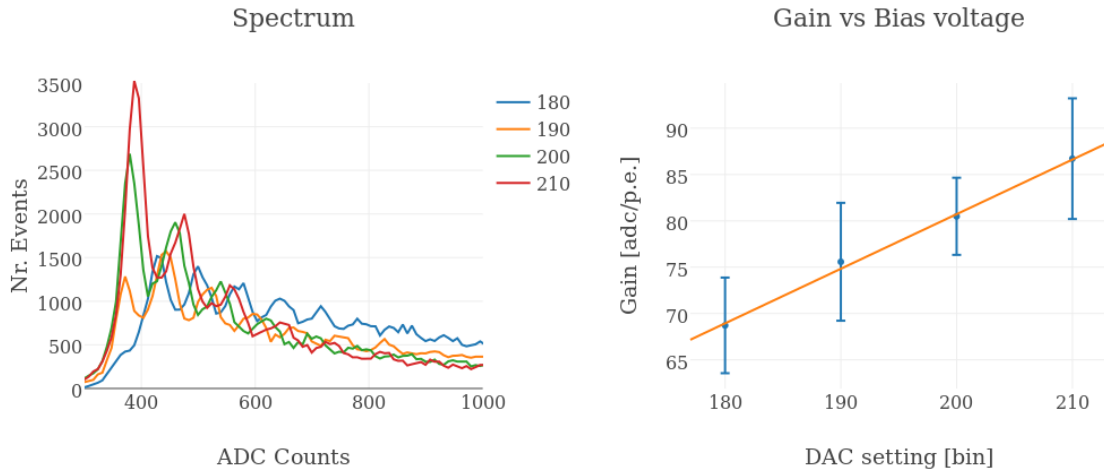
$$\propto V_{\text{over voltage}}, \quad (3)$$

where C_{cell} is the capacitance of a cell, e is the elementary electric charge, $V_{\text{breakdown}}$ is the breakdown voltage of the SiPM and V_{bias} is the bias voltage.

This relation lets the observed spectrum and the gain depend heavily on the bias voltage. A greater bias voltage leads to a greater charge stored in the SiPM's cells and therefore to a greater discharge when the cell interacts with a photon. This consequently leads to a higher gain.

The bias voltage of the SiPMs is generated by a manually trimmed stabilized power supply and a configurable DAC output voltage. Since the trimmed output varies from FEB to FEB and the effective parameter used to calibrate the CRTs is the DAC's setting, the gain is computed in dependence of the digital setting of the DAC. The spectral change is displayed in figure 35.

V_{bias} is greater than $V_{\text{breakdown}}$ for SiPMs running in Geiger mode



To determine this dependency, the bias voltage is changed by changing the setting responsible for the DAC's output – recall figure 28. For every DAC setting, several sets of observations are made, the resulting relation is visible in figure 35. Even if the uncertainty of the gain is high at every observation point, a linear dependency can be guessed.

Figure 35: The plot on the left displays spectra of a SiPM for increasing bias DAC output. It is clearly visible, that the spectrum shifts to the right with greater DAC setting. It is also visible, that the distance between the peaks increases with greater DAC setting. The plot on the right displays the dependence of the gain on the DAC setting.

The spectra of an uncalibrated panel vs. a calibrated panel

The observed spectra vary from SiPM to SiPM. For ideal components, fixing the bias voltage to a certain value for all SiPMs solves the problem. In the case of real components a change in the spectrum is clearly visible, as displayed in figure 36.

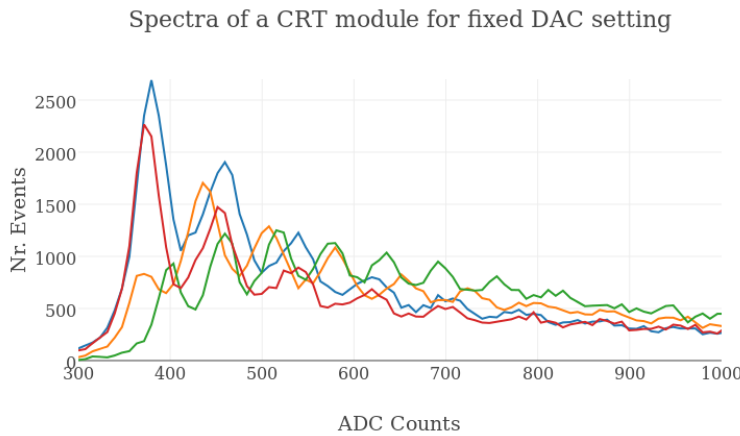


Figure 36: The spectra of 4 channels of the same CRT module are displayed. Every color represents one of the observed channels.

The gains of the SiPMs are computed and displayed in the left plot of figure 38 to visualize the distribution of gains in within a CRT module for fixed bias voltages.

With the aim to improve the spread of gains within a CRT module and improve therefore the uncertainty of the gain, the dependency of the gain on the bias voltage is computed for every SiPM of the CRT module. The obtained curves are plotted in figure 37.

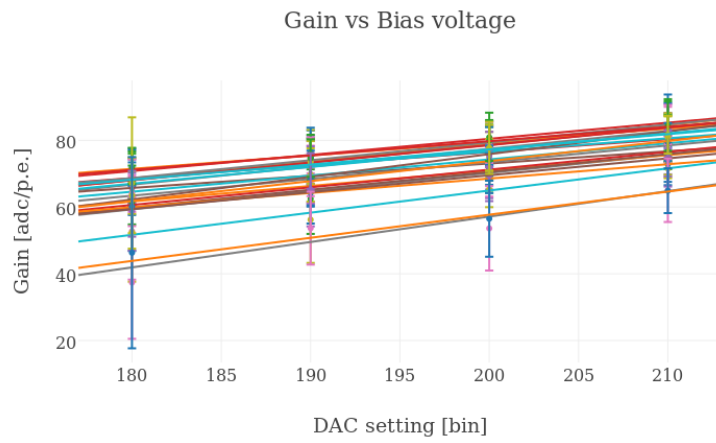


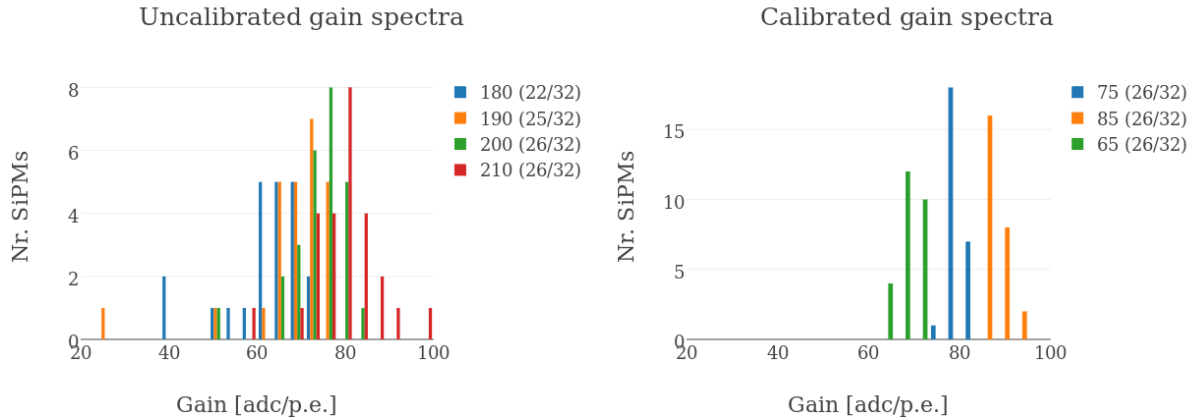
Figure 37: Change in gain in dependency of the DAC setting. Every colored line represents a different channel.

The inclination of the resulting slopes are similar for all the SiPMs. The interval of configurable gains is narrow in within the given range of bias settings. Due to the spread of the slope's position the interval of achievable gains for an uniform distribution is further reduced.

Using the computed dependencies and a simplified version of relation 1 the settings for the biasing DAC is computed for every SiPM, with the aim to reduce the dispersion of gains within a module.

To test the sensitivity of the calibration, the bias settings are computed for three different gain within the attainable range: 75, 85 and 65 ADC counts per photo electron. A set of observations is made for every set of computed settings and the gains are computed and counted for every SiPM. The distributions are displayed in the right plot of figure 38.

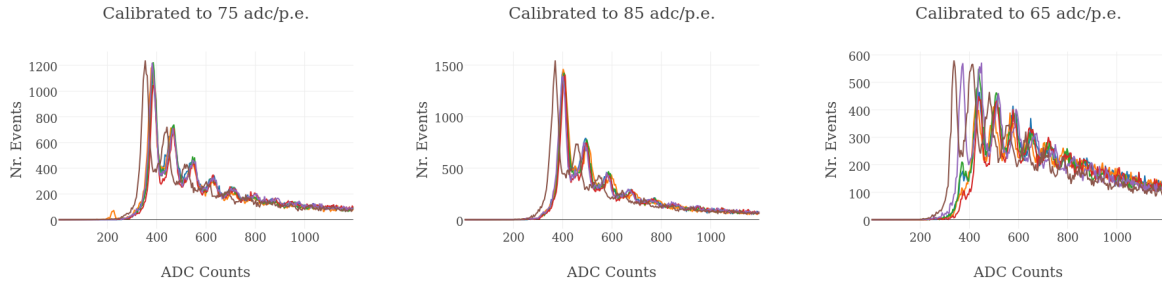
$$G = a \cdot \text{bias} + b \rightarrow \text{bias} = \frac{G-b}{a}$$



An important reduction of the spread of gains is observable in the plots of figure 38.

For comparison with the uncalibrated spectra, the observed spectra for fixed nominal gains are displayed in figure 39.

Figure 38: The plot on the left shows the spectrum of computed gains for fixed DAC settings for every SiPM. The plot on the right displays the distribution of gains after the calibration process. To make the change more visible, the same range for the x axis is used.



An improvement in the spectra's uniformity in comparison to the uncalibrated spectra shown in figure 36 is visible.

Figure 39: Observed spectra after calibration process.

Further studies on the Cosmic Ray Tracker

Using the software bundled with the FEB and CalibRaTe, 3 further sets of observations are made to analyse the behaviour of the CRT modules, test the functionality of the data acquisition software and show the versatility of the evaluation tools. This section lists the observations made with the CRT modules and analyzes part of the data of the observation sets.

Sets of observations

The FEB's power supply voltage affects the generation of the bias voltage V_{bias} and the output of the discriminator used to determine the threshold. A change in the power supply voltage will changes the visible spectrum in the histograms. Several sets of measurements have been taken using different power supply voltages to see this behavior and other effects. The set of parameters for these observations are listed in table 3.

Date	FEB & panels	Power supply voltage [V]				
2016-07-30		4.50	4.60	4.70	...	5.10
2016-08-03	(71, 371)			5.20		
2016-08-04		5.30	5.40	5.50		

The used data acquisition software was written to read data from several modules in parallel. Another feature of the software is to permit the acquisition of data for a set of DAC settings without human interaction. To test this functionality, the set of observations OS2 – listed in table 4 was made.

Date	FEBs & panels	DAC setting [bin]				
	(75, 375) (76, 376)					
2016-08-07	(77, 377) (78, 378)	180	181	182	...	200
	(79, 379) (80, 380)					

Table 3: Parameters of the observation set OS1. The FEB was powered with a Gw Instek GPS-4304 Power Supply, the power supply voltage's value was set manually and checked with a Fluke 115 Multimeter with an uncertainty of 0.01V. The power supply displayed a constant current at 0.52 (0.01) A.

Table 4: Parameters of the observation set OS2. The FEB was powered with rack power supply, the power supply voltage was kept constant at 4.63 (1) V and checked with a Fluke 115 Multimeter.

Effects of changing power supply voltages on the pedestal

A gaussian distribution is fitted around the pedestal of every SiPM for every parameter of observation set OS1. The resulting positions, width and amplitudes are plotted in dependency of the power supply voltage in figure 40.

The correlation of the signal of the 32 SiPMs is evident. The plot also shows, that the pedestal of the CRT module has at least two different 'regimes'. Notice the change of all three parameters at power supply voltages at and around 4.7V and 5.1V. The pedestal changes by $\approx 10\%$, while the width and amplitude change by a factor of 2. The reason for this behaviour requires further study.

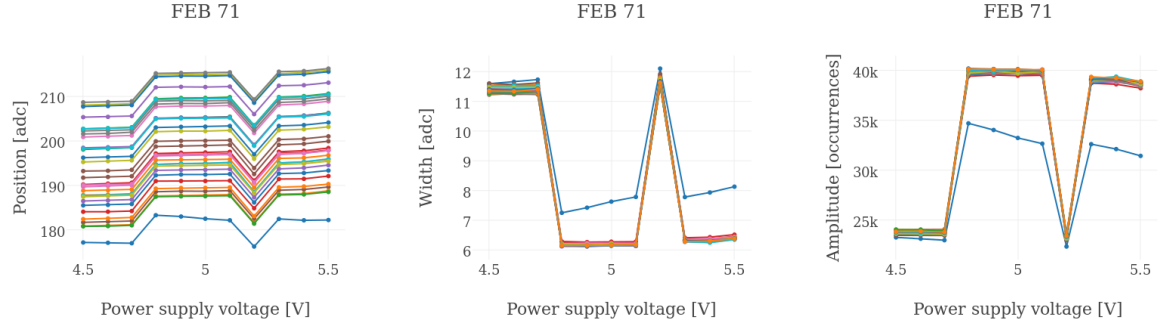


Figure 40: Fitted pedestal positions for the 32 SiPMs of observation set OS1. Every colored line represents a SiPM of the CRT module. The uncertainties of the fits are tiny and not displayed in the plot.

Influences of the power supply voltage on the spectrum

The behaviour of the spectrum is observed for changing power supply voltages, using the data from set OS1. The spectrum of a SiPM is displayed in dependency of the power supply voltage in figure 41.

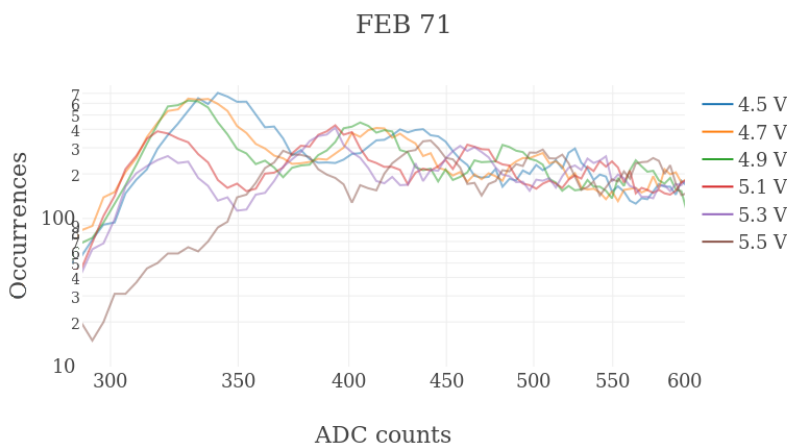


Figure 41: Observed spectrum for changing power supply voltages. A shift of the spectrum to the left is clearly visible with increasing power supply voltage.

The figure shows the spectrum of a SiPM for varying power supply voltages. It is clearly visible, that the spectrum depends on the power supply voltage. It is not obvious, though expected, that the distance between peaks change. The shift of the spectrum to the left with raising voltage is undeniable. This behavior shows the importance of a stable power supply voltage.

Event rate vs. power supply voltages

During DAQ an important change of the time spent to acquire the same amount of data was noticed. To study this behavior further, the FEB's event rates were observed and stored using the output of the monitoring software febmon. Since febmon does not specify which SiPM originates the observed event rate, spectra of the event rates are generated. The event rate spectrum for every voltage is plotted histogram 42.

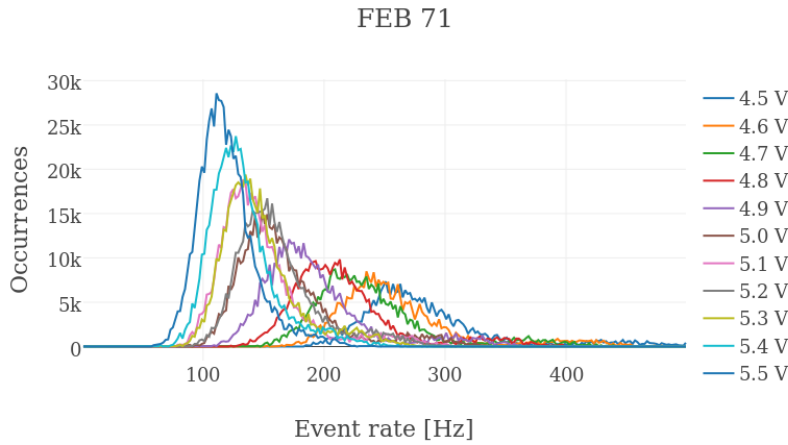
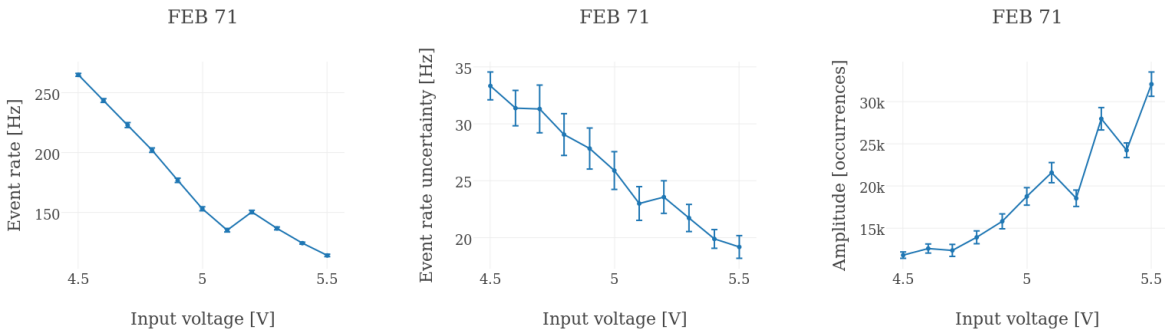


Figure 42: Observed spectra of the event rates for FEB 71 and panel 371 for different power supply voltages. The shift to the left with increasing power supply voltage is evident.

The plot shows gaussian distributed spectra, whose shape and position depend clearly on the power supply voltage. The distribution shifts to the left with increasing power supply voltage while getting thinner and gaining amplitude.

To see this effect more clearly, a gaussian distribution is fitted to each spectrum to determine its amplitude, position and width. These fit parameters are plotted in dependence of the power supply voltage in figure 43 to see the dependency on the power supply voltage.



The decrease of the event rate with increasing power supply voltage is obvious. This decrease suggests a change in the detection efficiency. The dispersion of the event rate spectra within a CRT module decreases with higher voltage, consequently the amplitude of the gaussians increases with higher power supply voltage. Since the event rates decrease with higher voltage and each set of measurements contains the same amount of events, the time febmon observed the event rate increased. Due to febmon's constant observation rate, the number of observations and therefore the amplitude of the spectra increases with longer observation time.

Figure 43: Fit parameters (fltr: position, width and amplitude) of the event rate distributions in dependency of the power supply voltages.

Effects of changing bias voltages on the pedestal

Since the pedestal is an indicator of the noise in the signal, studying its behavior in dependency of the bias voltage is of importance. For this reason the pedestal is studied for the observation set OS2. The positions and widths of the fitted gaussians are displayed in figures 44 and 45.

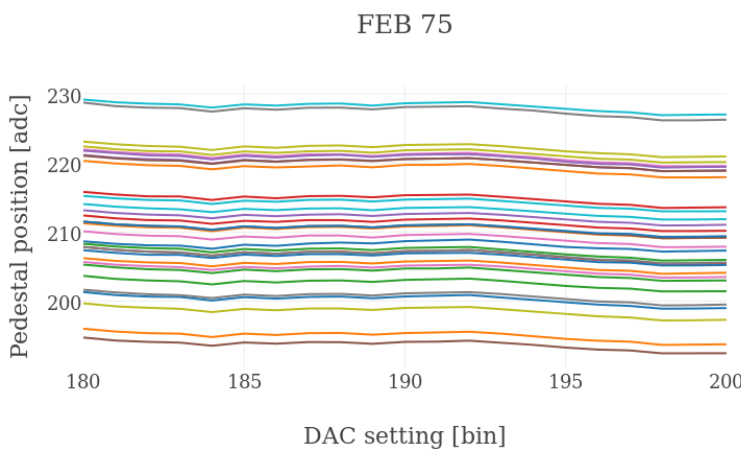


Figure 44: Fitted pedestal positions in dependency of the bias voltage for one of the FEB of a observation set OS2. Every colored line represents a SiPM of the module.

The plot displays a clear correlation of the pedestals change in position for all the SiPM signals. This correlation indicates the independency of the SiPM on the change of position, suggesting the FEB as main contributor to this parameter. This correlation is visible for all observed CRT panels. The positions of the pedestals depend on the SiPM. The spread of pedestal positions is assumed to be related to the spread of gains of an uncalibrated CRT module.

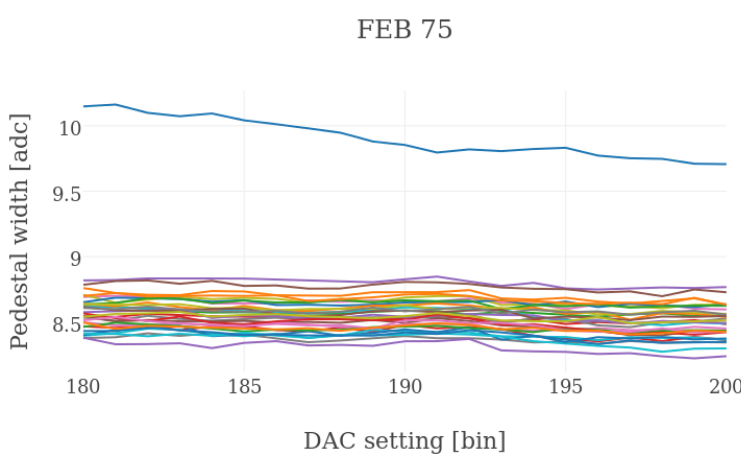


Figure 45: Fitted pedestal widths in dependency of the bias voltage for one of the FEB of a observation set OS2. The widths of the pedestals are similar to each other, only one of the SiPMs has a wider pedestal. Every colored line represents a SiPM of the module.

The width of the pedestal is similar for all the SiPMs of the same CRT module. Only one SiPM's pedestal is considerably wider than the rest. This behavior is attributed to the greater difference in voltage during digitizing process for the first SiPM which leads

to a greater uncertainty of the ADC's input. The width of the first SiPM's pedestal tends to decrease with increasing bias voltage.

The computed positions and widths of the pedestal are counted for all the sets of OS2 and displayed in figure 46.

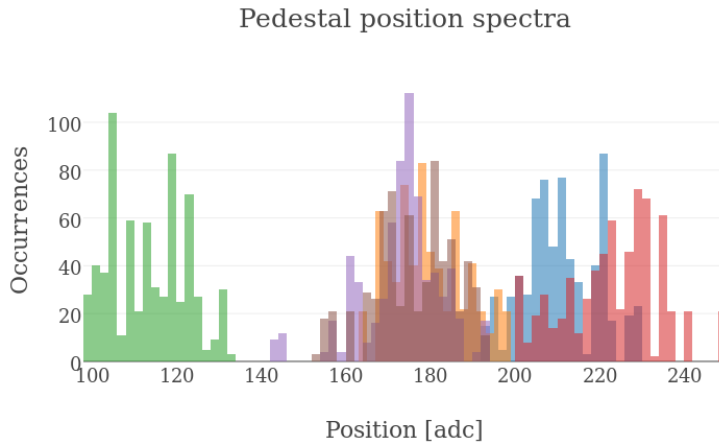


Figure 46: The spectra of the fitted positions of the pedestal for the observation set OS2. Every color represents a different CRT module.

The pedestals are distributed around a mean value which varies from CRT module to CRT module. The distribution of the pedestals give an idea of the variation of the pedestal.

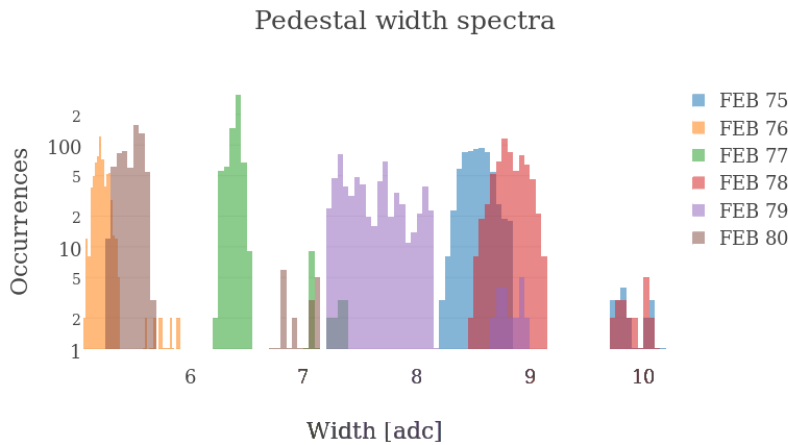
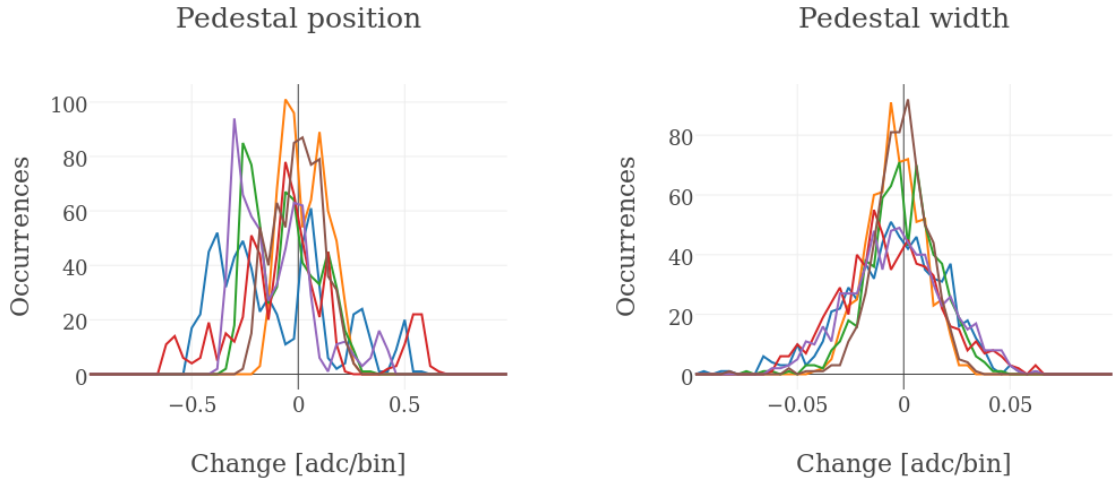


Figure 47: The spectra of the fitted widths of the pedestal for the observation set OS2. Each distribution contains the computed widths of all the SiPMs for all set bias voltages. Each color represents a different CRT module. A feature on the right of every distribution is visible, attributed to the first SiPM of every CRT module.

The figure displays a variety of distributions, whose mean and standard deviation depends heavily on the observed CRT module. The difference of the first SiPM's pedestal width is visible in each distribution.

The change of position and width of the pedestal is observed in dependency of the bias voltage, by computing and counting all the changes of the respective parameters. The resulting distributions are displayed in figure 48.

The computed spectra of the parameters' differences are distributed around the origin. The spectra of the pedestals' position is more spread than the spectra of the pedestals' width.



This study is done for a fixed power supply voltage. Since the power supply voltage influences the regime of the pedestal, a study including the variation of the power supply voltage and the bias voltage is recommended.

Figure 48: Histograms displaying the spectrum of changes in pedestal position, width and amplitude for observation set OS2.

Conclusions

The behavior of the amplitude spectrum obtained from several CRT modules under different bias voltages is studied and a method to determine a SiPM's gain is developed. The linear dependency of the gain on the bias voltage is been studied and used to elaborate a calibration method for the CRT modules. The improvement of the calibrated amplitude spectrum is significant.

The calibration of the gain is a tedious task, with many influences of many parameters. With the help of automated tools, human interaction can be reduced, making the calibration of the gain an affordable task.

The selection rules for the validity of the peaks in the fitting procedure can be improved to achieve smaller uncertainties. Including the second and third most frequent distance between the peaks to reduce the gain's uncertainty needs to be studied.

The additional studies indicate an important dependency of the spectrum on the power supply voltage. This effects need to be taken into consideration during and after CRT module calibration.

The study of the calibration results for varying power supply voltages is recommended.

The computed gains and bias settings of the calibration of the CRT module 75 is found in table 5.

Aimed gains	75			85			65		
	SiPM	bias	gain	SiPM	bias	gain	SiPM	bias	gain
0	192	77.5 (7.4)		0	209	87.9 (5.7)	0	174	70.6 (3.2)
1	195	81.8 (2.6)		1	219	91.8 (6.2)	1	172	67.5 (7.3)
2	192	81.3 (8.3)		2	211	89.8 (5.9)	2	173	68.2 (6.2)
3	194	79.4 (5.2)		3	212	88.3 (4.5)	3	176	69.8 (5.7)
4	196	80.5 (5.4)		4	221	92.8 (5.4)	4	171	65.6 (7.1)
5	188	77.9 (7.0)		5	212	88.3 (5.7)	5	164	65.8 (6.4)
6	189	79.6 (5.1)		6	208	87.9 (5.5)	6	169	65.0 (12.1)
7	205	81.3 (6.4)		7	233	95.0 (5.2)	7	177	67.8 (12.4)
8	207	77.8 (3.4)		8	227	86.4 (3.6)	8	188	68.8 (2.1)
9	201	80.8 (5.1)		9	222	88.9 (5.8)	9	181	72.1 (6.4)
10	209	79.8 (3.8)		10	231	89.3 (3.6)	10	186	64.3 (8.0)
11	206	79.6 (3.1)		11	225	87.1 (7.3)	11	188	71.1 (3.6)
12	207	78.8 (6.3)		12	226	88.7 (4.4)	12	188	69.4 (3.3)
13	203	78.6 (3.0)		13	223	88.4 (7.4)	13	183	69.5 (2.6)
15	215	76.4 (2.2)		15	234	85.8 (2.5)	15	196	67.6 (2.6)
18	215	81.1 (3.6)		18	237	88.4 (3.7)	18	192	69.1 (4.2)
19	193	78.9 (3.6)		19	211	88.0 (3.2)	19	175	69.8 (3.2)
20	199	80.9 (3.2)		20	214	88.1 (3.6)	20	184	73.0 (2.8)
21	192	79.6 (4.1)		21	210	88.3 (4.7)	21	173	68.5 (8.8)
22	195	78.9 (4.8)		22	214	85.5 (4.2)	22	176	67.0 (6.9)
23	202	81.0 (5.6)		23	218	87.5 (7.9)	23	186	71.4 (4.7)
24	189	79.8 (5.5)		24	212	89.7 (4.4)	24	167	65.0 (10.7)
25	210	81.0 (6.5)		25	230	89.6 (4.1)	25	190	71.1 (2.5)
26	230	81.6 (3.9)		26	249	89.8 (4.4)	26	212	72.4 (8.3)
27	198	79.3 (3.6)		27	214	87.8 (6.6)	27	181	71.6 (7.3)
30	217	78.2 (4.0)		30	235	87.6 (2.2)	30	198	67.0 (5.5)

Table 5: Results of the calibration of CRT module 75 for a power supply voltage of 5.5 (0.1) V. The resulting settings for the bias changing DAC and corresponding computed gains are listed for the three aimed gains. The gain is given in ADC counts per photo-electron.

Bibliography

- TSpectrum class reference. <https://root.cern.ch/doc/master/classTSpectrum.html>. Accessed: 2016-09-09.
- Root data analysis framework. <https://root.cern.ch>. Accessed: 2016-09-09.
- M. G. Aartsen et al. Observation and characterization of a cosmic muon neutrino flux from the northern hemisphere using six years of icecube data. 2016.
- T. Adam et al. Measurement of the neutrino velocity with the opera detector in the cngs beam. *JHEP*, 10:093, 2012.
- M. Antonello et al. Precision measurement of the neutrino velocity with the icarus detector in the cngs beam. *JHEP*, 11:049, 2012.
- M. Antonello et al. A proposal for a three detector short-baseline neutrino oscillation program in the fermilab booster neutrino beam. 2015.
- M. Auger, A. Ereditato, D. Goeldi, I. Kreslo, D. Lorca, M. Luethi, C. Rudolf von Rohr, J. Sinclair, and M. S. Weber. Multi-channel front-end board for sipm readout. 2016.
- John Bahcall. Solving the mystery of the missing neutrinos, April 2004. URL http://www.nobelprize.org/nobel_prizes/themes/physics/bahcall/.
- A. Bellerive, J. R. Klein, A. B. McDonald, A. J. Noble, and A. W. P. Poon. The sudbury neutrino observatory. *Nucl. Phys.*, B908:30–51, 2016. DOI: [10.1016/j.nuclphysb.2016.04.035](https://doi.org/10.1016/j.nuclphysb.2016.04.035).
- G. Bellini, A. Ianni, L. Ludhova, F. Mantovani, and W. F. McDonough. Geo-neutrinos. *Progress in Particle and Nuclear Physics*, 73:1–34, November 2013. DOI: [10.1016/j.ppnp.2013.07.001](https://doi.org/10.1016/j.ppnp.2013.07.001).
- Brown, L. M. The idea of the neutrino. *Physics Today*, 31:23–28, sep 1978.
- M. T. Dova. Ultra-high energy cosmic rays. In *Proceedings, 7th CERN-Latin-American School of High-Energy Physics (CLASHEP2013): Arequipa, Peru, March 6-19, 2013*, pages 169–190, 2015. DOI: [10.5170/CERN-2015-001.169](https://doi.org/10.5170/CERN-2015-001.169). URL <https://inspirehep.net/record/1452529/files/arXiv:1604.07584.pdf>.
- Patrick Eckert, Rainer Stamen, and Hans-Christian Schultz-Coulon. Study of the response and photon-counting resolution of silicon photomultipliers using a generic simulation framework. 2012. DOI: [10.1088/1748-0221/7/08/Po8011](https://doi.org/10.1088/1748-0221/7/08/Po8011).
- Antonio Ereditato. The discovery of the appearance of $\nu_\mu \rightarrow \nu_\tau$ neutrino oscillations. *Nuclear Physics B*, 908:116 – 129, 2016. ISSN 0550-3213. DOI: <http://dx.doi.org/10.1016/j.nuclphysb.2016.03.014>.

- URL <http://www.sciencedirect.com/science/article/pii/S055032131600105X>. Neutrino Oscillations: Celebrating the Nobel Prize in Physics 2015.
- Frederick Reines. Nobel Lecture: The Neutrino: From Poltergeist to Particle, dec 1995. URL http://www.nobelprize.org/nobel_prizes/physics/lauriates/1995/reines-lecture.html.
- S. N. Glinenko. The miniboone anomaly and heavy neutrino decay. *Phys. Rev. Lett.*, 103:241802, 2009. DOI: 10.1103/PhysRevLett.103.241802.
- Herrero, M. The Standard model: Techniques and Concepts of High-Energy Physics. *NATO Sci. Ser. C*, 534:1–59, 1999.
- D. Karlen. The number of light neutrino types from collider experiments. 2004.
- Teppei Katori and Janet Conrad. Beyond standard model searches in the miniboone experiment. *Adv. High Energy Phys.*, 2015:362971, 2015. DOI: 10.1155/2015/362971.
- Paolo Maestro. Cosmic rays: direct measurements. *PoS*, ICRC2015: 016, 2015.
- K. A. Olive et al. Review of Particle Physics. *Chin. Phys.*, C38:090001, 2014. DOI: 10.1088/1674-1137/38/9/090001.
- E. Richard et al. Measurements of the atmospheric neutrino flux by super-kamiokande: energy spectra, geomagnetic effects, and solar modulation. 2015.
- R. Romero. On the nature of the neutrino. *Mod. Phys. Lett.*, A31(19), 2016.
- I. Sahin. A hypothesis on neutrino helicity, 2015.
- C. S. Wu, E. Ambler, R. W. Hayward, D. D. Hoppes, and R. P. Hudson. Experimental test of parity conservation in beta decay. *Phys. Rev.*, 105:1413–1415, Feb 1957. DOI: 10.1103/PhysRev.105.1413. URL <http://link.aps.org/doi/10.1103/PhysRev.105.1413>.
- Zhi-zhong Xing and Ye-Ling Zhou. Majorana CP-violating phases in neutrino-antineutrino oscillations and other lepton-number-violating processes. *Phys. Rev.*, D88:033002, 2013. DOI: 10.1103/PhysRevD.88.033002.

Declaration of consent

on the basis of Article 28. para. 2 of the RSL05 phil.-nat.

Last / First name	Vergés Pablo
Matriculation Nr.	04-812-269
Study program	Master
Title of thesis	SiPM Gain calibration for the scintillating Cosmic Ray Tracker
Supervisor	Prof. Dr. Igor Kreslo

I declare herewith that this thesis is my own work and that I have not used any sources other than those stated. I have indicated the adoption of quotations as well as thoughts taken from other authors as such in the thesis. I am aware that the Senate pursuant to Article 36 para. 1 lit. r of the University Act of 5 September, 1996 is authorised to revoke the title awarded on the basis of this thesis. I allow herewith inspection in this thesis

Place / Date

Signature